

High-fidelity entanglement and coherent multi-qubit mapping in an atom array

Aruku Senoo,¹ Alexander Baumgärtner,¹ Joanna W. Lis,¹ Gaurav M. Vaidya,¹
Zhongda Zeng,^{2,3} Giuliano Giudici,^{2,3} Hannes Pichler,^{2,3} and Adam M. Kaufman^{1,*}

¹*JILA, University of Colorado and National Institute of Standards and Technology,
and Department of Physics, University of Colorado, Boulder, Colorado 80309, USA*

²*Institute for Theoretical Physics, University of Innsbruck, Innsbruck A-6020, Austria*

³*Institute for Quantum Optics and Quantum Information,
Austrian Academy of Sciences, Innsbruck A-6020, Austria*

(Dated: November 27, 2025)

Neutral atoms in optical tweezer arrays possess broad applicability for quantum information science, in computing [1–3], simulation [4–6], and metrology [7–9]. Among atomic species, Ytterbium-171 is unique as it hosts multiple qubits, each of which is impactful for these distinct applications [10–15]. Consequently, this atom is an ideal candidate to bridge multiple disciplines, which, more broadly, has been an increasingly effective strategy within the field of quantum science [16–22]. Realizing the full potential of this synergy requires high-fidelity generation and transfer of many-particle entanglement between these distinct qubit degrees of freedom, and thus between these distinct applications. Here we demonstrate the creation and coherent mapping of entangled quantum states across multiple qubits in Ytterbium-171 tweezer arrays. We map entangled states onto the optical clock qubit [20, 23–25] from the nuclear spin qubit [10, 11, 26] or the Rydberg qubit [27, 28]. We coherently transfer up to 20 atoms of a Z_2 -ordered Greenberger-Horne-Zeilinger (GHZ) state [29] from the interacting Rydberg manifold to the metastable nuclear spin manifold. The many-body state is generated via a novel disorder-robust pulse in a two-dimensional ladder geometry. We further find that clock-qubit-based spin detection applied to Rydberg and nuclear spin qubits facilitates atom-loss-detectable qubit measurements and $> 90\%$ Rydberg decay detection [12–14]. This enables mid-circuit and delayed erasure detection, yielding an error-detected two-qubit gate fidelity of 99.78(4)% [14, 30] in the metastable qubits. This error detection also enables Rydberg qubit evolution with an effective lifetime of 1.2(2) ms, enhancing the fidelity of the observed many-body dynamics. These results establish a versatile architecture that advances multiple fields of quantum information science while also establishing bridges between them.

Quantum technologies are advancing along parallel tracks, with breakthroughs in computation [2, 31–34], simulation [35, 36], and metrology [15, 16]. Typically, each realization is driven by a specific qubit — a fundamental unit of quantum information — optimized to a particular task. For instance, a qubit optimized for sensing is unlikely to be ideal for quantum computing, as the sensitivity of the former compromises the robustness of the latter. However, combining such distinct functionalities unlocks a variety of new possibilities. Digital quantum gates can enhance access to observables previously challenging to measure for analog quantum simulations [17, 18, 37]; non-classical states generated through computation or simulation can be mapped onto ultranarrow optical transitions for quantum-enhanced metrology [16, 22, 23, 38]; and, computing-inspired error mitigation methods can be translated to quantum simulation and metrology [39–41].

In this context, favorable features of optical-tweezer-trapped neutral atoms — including isolation, scalability, and precision control — have found utility in multiple directions in quantum science, making it a promising platform to explore such synergies. These features, along with the non-local connectivity afforded by mobile optical tweezers, offer a promising framework for quantum

computing [1, 2, 42, 43], while their flexible geometry and tunable interactions are enabling for quantum simulation [4–6]. Additionally, the ability to isolate single atoms close to the motional ground state in a collision-free manner makes them well suited for metrology [7–9].

Among atomic species, Ytterbium-171 (^{171}Yb) is notable for its unique atomic level structure (Fig. 1a), which supports multiple qubits [13]. For quantum computation and memory applications, the spin 1/2-nuclear spin qubit, hosted in both the ground (g) and metastable (m) electronic states, is particularly attractive due to its long coherence times of up to 10 seconds [13], arising from the absence of hyperfine interactions with orbital electrons [10, 11, 13, 44]. The transition connecting the ground and metastable state (the optical qubit, o) is the basis of world-leading optical atomic clocks [15]. The single-photon transition between the metastable clock state and $^3\text{S}_1$ Rydberg series (r -qubits) enables high-fidelity entanglement generation [12, 21, 25, 28, 45–47]. And, most importantly, these different qubits can cooperate effectively: Rydberg interactions can be used to engineer entanglement in any of these qubits via digital or analog protocols, while the clock qubit allows loss-detectable spin measurements, which can be leveraged for enhanced fidelity [13]. Despite the broad potential, so far, combining all of these capabilities has yet to be achieved.

In this work, we demonstrate the full realization of

* e-mail: adam.kaufman@colorado.edu

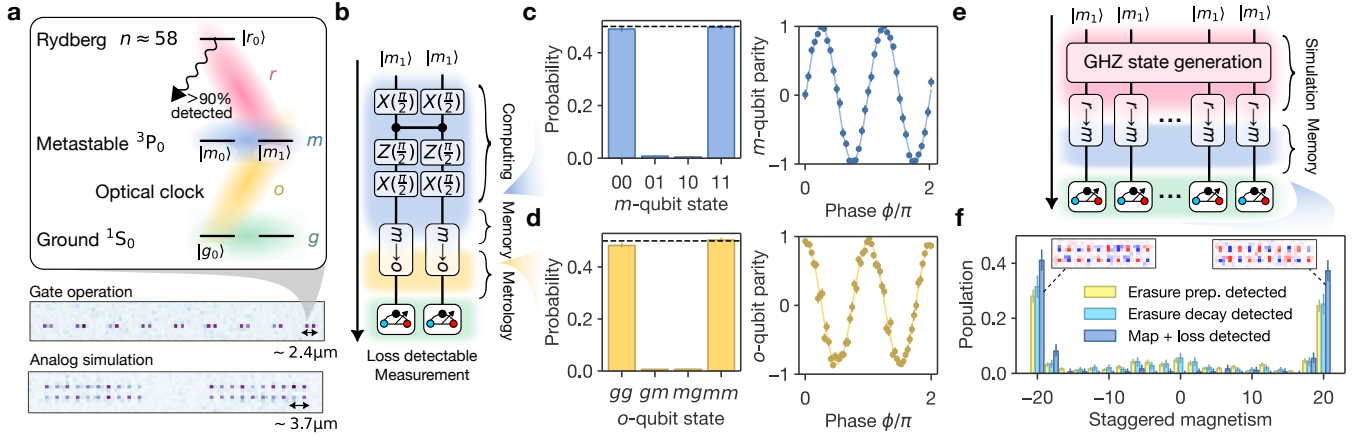


Fig. 1. **Architecture based on multi-level qubit mapping.** **a**, Schematic of the ^{171}Yb atomic structure (top panel). Coherent spin-1/2 nuclear spin qubit in both the ground state (g -qubit, green) and the metastable state (m -qubit, blue). An optical transition connects the ground and metastable states, defining the clock qubit (o -qubit, yellow). The $m_F = +1/2$ metastable state can be excited to a Rydberg level via a single photon transition at 302 nm (r -qubit, red). In this system, $> 90\%$ of Rydberg decay events are detected as atom loss. The bottom panel shows single-shot images after rearrangement for experiments involving two-qubit gates and experiments using analog many-body Hamiltonian evolutions. **b**, Bell state generation and mapping sequence. The Bell state generated by a high-fidelity two-qubit gate in the m -qubit manifold is subsequently mapped onto the o -qubit and detected by loss-detectable spin-measurements represented by a box with three dots. **c**, Measured m -qubit Bell state population (left) and the parity oscillation (right) with loss detection. **d**, Analogous measurement for o -qubit. **e**, The sequence of the GHZ-state mapping from r -qubit to m -qubit. The GHZ state is generated by an adiabatic many-body Hamiltonian sweep in the r -qubit and mapped to m -qubit. **f**, Measured Z_2 -order of the GHZ state. The staggered magnetism is defined as a sum of the magnetism with flipped signs for the nearest neighbor atoms (Methods). Three spin detection methods are compared. Yellow (left) shows the data of direct r -qubit spin detection with erasure detection to suppress preparation errors (Methods). Light blue (center) includes additional error detection through erasures revealed after the sequence, which identifies Rydberg-state decay events. Finally, dark blue (right) applies qubit mapping and loss detection, as shown in e. The observed Z_2 population is 53(3)%, 57(4)%, and 78(3)% respectively, showing two-fold improvement of population error in the loss detected case. (Inset) Single-shot loss-detected measurement result; images for two spins are combined with blue (red) color for $|m_0\rangle$ ($|m_1\rangle$).

this integration. Specifically, we create clock-qubit entangled states, generated either by two-qubit gates on the metastable state (Fig. 1b) or analog Hamiltonian evolution. Extending this capability to large entangled states, we map Z_2 -ordered Greenberger-Horne-Zeilinger (GHZ) states of up to 20 atoms onto long-lived nuclear spin qubits (Fig. 1e). Notably, our near-adiabatic preparation of the GHZ state in a ladder geometry exploits a novel disorder-robust scheme [48] discovered via quantum optimal control techniques [49]. In all of these demonstrations, we exploit clock-shelving-based loss detection to each qubit type — interacting Rydberg qubits, nuclear-spin qubits, and clock qubits — leading to detection of $> 90\%$ of Rydberg decay errors during analog Hamiltonian evolution with effective Rydberg lifetime of 1.2(2) ms (Fig. 1f) and an error-detected two-qubit gate fidelity of 99.78(4)% with corresponding high-fidelity Bell-state generation (Fig. 1c). These results establish a versatile multi-qubit platform, providing a compelling new strategy to seamlessly integrate quantum computing, simulation, and metrology.

Multi-level qubit mapping and loss detection

We manipulate ^{171}Yb trapped in optical tweezer arrays in a two-dimensional ladder arrangement. The single atom arrays are prepared by combining $\sim 90\%$ enhanced loading and rearrangement [4, 10] (Extended Data Fig. 1 and Methods). For loading and rearrangement, we use 532 nm tweezer arrays. Atoms are then transferred to 767 nm tweezers close to the clock-magic wavelength (Extended Data Fig. 1 and Methods). In each experimental run, we initialize the atoms in the radial motional ground state and coherently excite them to the metastable state via the optical clock transition, while preserving their motional level [13].

Our study focuses on three distinct qubit types (Fig. 1a), out of 4 atomic levels: the $m_F = -1/2$ hyperfine state of the ground state 1S_0 ($|g_0\rangle$), the $m_F = \mp 1/2$ hyperfine states of the metastable 3P_0 ($|m_0\rangle$ and $|m_1\rangle$), and the $|\nu \approx 53.3, L = 0, F = 1/2, m_F = -1/2\rangle$ Rydberg state with $n \approx 58$ ($|r_0\rangle$) identified in [47]. The o -qubit widely employed in optical clock metrology consists of $|g_0\rangle$ and $|m_1\rangle$ [15]. We implement global single-qubit X -rotations for this qubit with a typical Rabi frequency of $2\pi \times 90$ kHz, while virtual Z -rotations are controlled

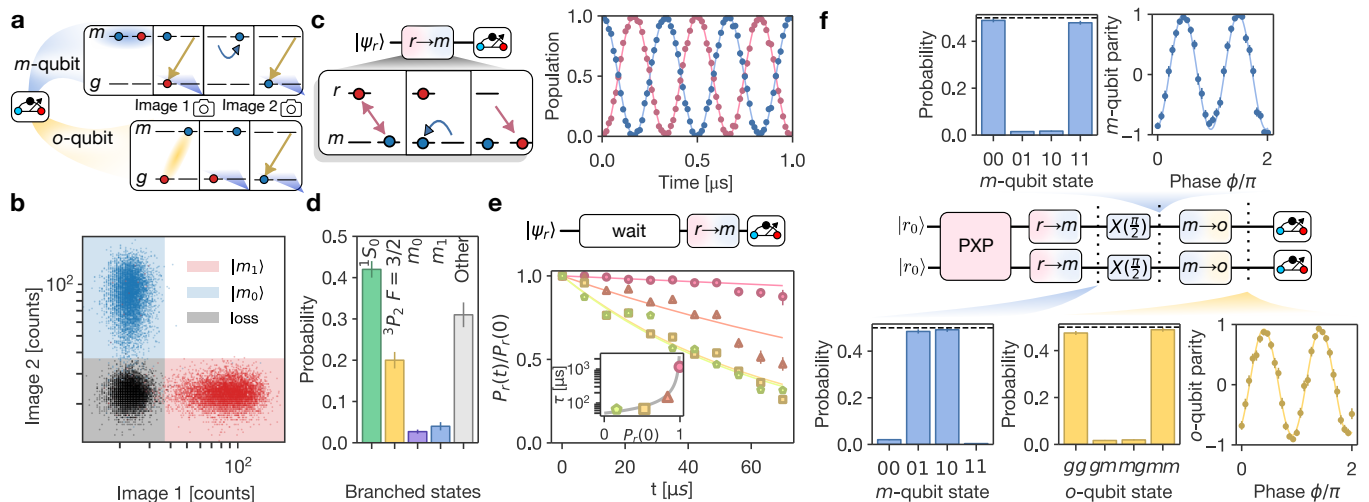


Fig. 2. Qubit mapping and loss-detectable spin measurement. **a**, Sequence of the loss-detectable spin measurements for the m -qubit (top) and the o -qubit (bottom). A clock π -pulse is used to selectively de-excite one of the spin components. Each spin component is destructively imaged via fast fluorescence imaging (see Methods). **b**, Distribution of the camera counts of the spin measurement. We apply the measurement to distinguish the three outcomes $|m_1\rangle$, $|m_0\rangle$, and atom loss, for the case of preparing each of these states (red, blue, and black dots). **c**, Loss-detectable spin measurement of r -qubit. The left schematic shows the sequence of mapping the r -qubit onto the m -qubit. (Right) Rabi oscillations of the Rydberg state observed by this spin-measurement method with loss detection. Both $|r_0\rangle$ population (red) and $|m_1\rangle$ population (blue) are observed simultaneously. **d**, Measured branching ratio of the decay for $|r_0\rangle$ Rydberg state (see Extended Data Fig. 5). Decays are registered as atom loss unless the atom decays back into the qubit manifold in use. **e**, Observation of population decay dynamics consistent with the non-Hermitian state evolution via qubit mapping and loss detection. The loss-detected probability of Rydberg state, $P_r(t)$ is plotted, where each marker represents different initial Rydberg populations, $\{16(1)\%, 53(2)\%, 84(1)\%, 99.7(3)\%\}$. The inset compares the fitted decay time constant and the curve derived from non-Hermitian dynamics without free parameters (see Methods). We use $P_r(t) = P_r(0)e^{-t/\tau}$ for the fitting function. **f**, Proof-of-concept demonstration combining analog quantum simulation and digital quantum operations to generate a metrologically valuable state. After evolving two atoms under the PXP-Hamiltonian, a Bell state in the Rydberg qubit is generated and mapped onto the m -qubit (lower left). A $\pi/2$ -pulse on the m -qubit then converts the $(|01\rangle + |10\rangle)/\sqrt{2}$ Bell state into a $(|00\rangle + |11\rangle)/\sqrt{2}$ Bell state (top), which is subsequently mapped onto the clock o -qubit (lower right).

with the optical phase. The m -qubit is encoded in the nuclear spin states $|m_0\rangle$ and $|m_1\rangle$ [11, 13], with X -rotations performed using optical Raman rotations [13]. To minimize the scattering error during the single-qubit operations, we employ phase tracking for Z -rotations where our qubit splitting is $2\pi \times 9.5$ kHz in the typical magnetic field of 8.2 G. Finally, the r -qubit is defined between $|m_1\rangle$ and $|r_0\rangle$. Using a 302 nm ultraviolet (UV) laser, we drive the qubit with a Rabi frequency of around $2\pi \times 3$ MHz via a single-photon excitation.

Fig. 1 visualizes the mapping of an entangled state. We first show the transfer of the entangled Bell state from the m -qubit to the o -qubit (see Fig. 1b). Using a high-fidelity two-qubit gate (detailed later), we generate the $(|00\rangle - i|11\rangle)/\sqrt{2}$ Bell state in the m -qubit manifold. The loss-detected fidelity of this Bell state is 98.6(3)% based on the average of the Bell state population, 98.7(2)%, and amplitude of parity oscillations, 98.4(6)% (Fig. 1c); we estimate 99.0(3)% Bell state fidelity after correcting for measurement errors (Methods). To transfer the entangled state to the o -qubit, we apply two consecutive π -pulses first to the o -, then the m -manifold. The loss-detected fidelity of the transferred Bell state results in

93.8(6)% with a population of 98.6(2)% and parity oscillation amplitude of 89.1(1)% (Fig. 1d). During the mapping to the o -qubit, tweezers are turned off to avoid differential light shift from the non-magic wavelength tweezer.

We exploit loss-detectable spin measurements of the metastable qubit for error detection, which have recently been developed in several qubit architectures in neutral atom platforms [13, 30, 41, 44, 50–52]. Here, we employ the selectivity of the polarization of the clock beam for hiding one of the states in the metastable manifold [13]. The sequential imaging of both atomic spin states allows measurement of both spin states as well as atom loss. While previous demonstrations concentrate on measuring g -qubit loss-detectably [13, 44, 51], we expand this to multiple qubits applying the mapping. Fig. 2a illustrates the detailed procedure for the spin measurement in both m -qubit and o -qubit. The distribution of the camera counts in Fig. 2b compares the three situations where atoms are prepared in $|m_0\rangle$ or $|m_1\rangle$ and no atom is prepared. From this, the average spin-detection infidelity is deduced as 0.44(6)%, while the False-Positive rate of the loss detection is 3.6(1)% due to the extra loss induced during the measurement process (see Extended

Data Table. I and Methods).

The loss-detectable spin measurement can be extended to the r -qubit by mapping the r -qubit spin state onto the m -qubit. Fig. 2c illustrates this procedure, which consists of a π -pulse on the m -qubit followed by a π -pulse on the r -qubit before doing the m -qubit spin measurement. To mitigate the effect of dephasing the r -qubit during this process, the m -qubit rotation must be much faster than the coherence time of the Rydberg state. In this experiment, the T_2^* coherence time is $12.8(5) \mu\text{s}$ and the Rydberg decay time constant is $46(2) \mu\text{s}$ (see Extended Data Fig. 4 and Methods). By using the smaller intermediate state detuning of our two operation modes, we achieve a $0.19 \mu\text{s}$ π -pulse duration of m -qubit X rotation, a comparable speed to the r -qubit π -pulse of $0.15 \mu\text{s}$ (see Extended Data Fig. 3 and Methods). This suppresses the estimated Rydberg decayed population during the process to below 0.5% per atom. The right panel of Fig. 2c shows Rabi oscillations on the r -qubit measured with this scheme, where the amplitude contrast is observed to be as high as 99.6(3)%, due to the mitigation of preparation errors and high-fidelity control of the Rydberg state (see Extended Data Fig. 4 and Methods).

The loss-detectable r -qubit spin measurement is naturally applied to detect the decay of the Rydberg state, as most decay pathways lead to loss. The fidelity of the decay detection is governed by the branching ratio of the Rydberg state, presented in Fig. 2d. For experiments based on the r -qubit, since we use $|r_0\rangle$ and $|m_1\rangle$, our Rydberg decay detection fidelity is 96(1)% after the application of the resonant scattering beam to remove any ground state population. Also, the fact that the $^3\text{P}_2$ metastable state is highly anti-trapped in our 767 nm tweezers prevents them from decaying back to the ground state manifold during the spin read-out. For the experiment involving both m -qubit and r -qubit, such as the two-qubit gate experiments, the decay detection fidelity reduces to 93(1)%, accounting for the combined decay rates to $|m_0\rangle$ and $|m_1\rangle$. However, because this loss-detection-based method is effective to additional populations that do not decay (or get repumped) to the ground state, it leads to a significant improvement in the total fraction of detected erasures relative to previous experiments [12, 14, 45], at the price of delayed information arrival until qubit detection is performed.

The high fraction of detected decay events can reveal the non-Hermitian state evolution of a decaying quantum system [53]. As a simple example, we observe the effective population evolution of superposition between a decaying $|r_0\rangle$ state and a non-decaying $|m_1\rangle$ state. By preparing a coherent superposition $|\psi_r\rangle = \sqrt{1 - |a|^2} |m_1\rangle + a |r_0\rangle$, which has a Rydberg fraction of $|a|^2$, we investigate how the Rydberg state population, $P_r(t)$, evolves in experiments where Rydberg decay is not detected. When the initial population is entirely in the Rydberg state, the effective population decay is suppressed. However, as the portion of $|m_1\rangle$ increases, we detect an accelerated decay rate of this population, illustrating that even without ob-

serving the decay, the populations evolve (Fig. 2e). We compare our observation with the expected behavior of the non-Hermitian evolution, which shows good agreement (Fig. 2e inset and Methods). The observed slow decay time constant of $1.2(2) \text{ms}$ for the pure Rydberg atom case ($P_r(0) = 1$) indicates the fidelity of the decay detection is 96.1(7)%, consistent with the estimate from the branching ratios.

To further illustrate the flexibility of the multi-qubit mapping, we demonstrate the transfer of the r -qubit Bell state to the m -qubit and then to the o -qubit, conceptually illustrating the combination of quantum simulation, quantum computation, and quantum metrology (Fig. 2f). In the highly Rydberg-blockaded regime, two atoms evolve according to the ideal PXP model Hamiltonian, generating the $(|mr\rangle + |rm\rangle)/\sqrt{2}$ Bell state in the r -qubit [4]. We halt the evolution at this point, and map the r -qubit state to the m -qubit. By applying a $X \pi/2$ -pulse to the $(|01\rangle + |10\rangle)/\sqrt{2}$ Bell state in the m -qubit, we generate the metrologically-useful $(|00\rangle + |11\rangle)/\sqrt{2}$ Bell state, where the loss-detected fidelity is measured to be 96.3(8)% with population of 96.8(3)% and parity oscillation amplitude of 95.8(1.5)%. Finally, we map the m -qubit Bell state to the o -qubit, reaching 92.4(9)% fidelity with 96.4(3)% population and 88.3(1.8)% parity oscillation amplitude.

Rydberg-mediated two-qubit gates with loss detection

Applying the loss- and Rydberg-decay-detection, we demonstrate high-fidelity two-qubit gates [14, 30] and studies of unique errors arising during the Rydberg-blockade dynamics underlying the gate. We employ a time-optimal gate (TOG) protocol [54, 55], sinusoidally modulating the optical phase of the driving laser. To evaluate the two-qubit gate fidelity separate from SPAM errors and single-qubit errors, a global randomized benchmarking (gRB) is implemented [12, 14, 30, 46, 47, 55]. We alternate randomly chosen single-qubit Clifford gates with two-qubit gate operations, and the final four single-qubit gates, R_1, R_2, R_3, R_4 , are chosen such that both qubits return to their initial state. Importantly, we also apply an ionization pulse after each CZ gate to convert residual Rydberg population after the gate to (detectable) loss.

With this approach, we extract a raw gate fidelity of 99.37(7)% (see Methods). While detection of Rydberg decay via the ground-state population improves the fidelity to 99.51(6)%, loss detection further improves the fidelity, observing 99.78(4)% two-qubit gate fidelity. The relative improvement in fidelity using erasure decay detection compared to loss detection implies a branching ratio to the ground state that is consistent with the directly measured one shown in Fig. 2d. We also observe a consistent loss-detected fidelity of 99.75(4)% when including an echo (Methods), which suggests that the mea-

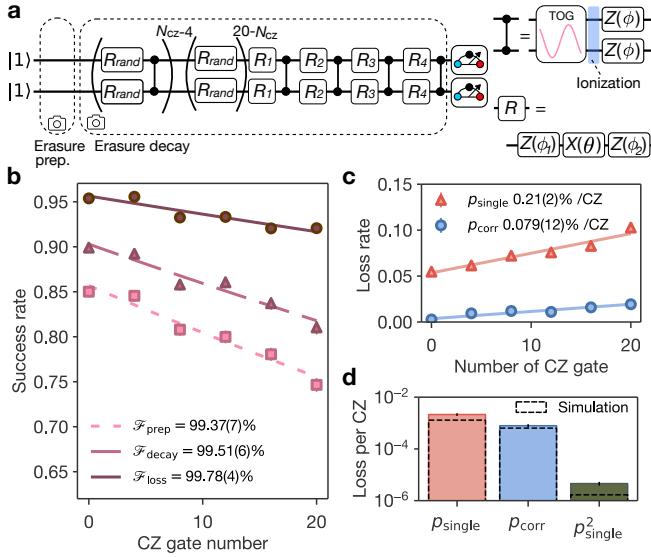


Fig. 3. **High-fidelity two-qubit gate enhanced by loss detection.** **a**, Global randomized benchmarking (gRB) sequence. To compare to the loss detection, ground state erasure detection is implemented. Preparation errors in the metastable state are detected by observing the ground state population at the beginning of the gRB sequence, while some of the qubit leakage errors are continuously monitored by observing the ground state population during the sequence. The erasure detection beam is off only during the two-qubit gate operations. **b**, gRB results. We observe an increase in the gate fidelity by partially detecting the decayed population by erasure decay detection (triangle) compared to the case only with preparation erasure detection (square). With loss detection, the fidelity increases to 99.78(4)% (circle). **c**, Atom loss in the gRB experiment after preparation erasure detection. Here, the loss includes auto-ionized population due to the remaining population in the Rydberg state after a gate. **d**, Histogram of measured loss per CZ gate. The dashed line shows the simulation result (Methods).

sured gate fidelity with loss detection is independent of the benchmarking method. This achieved gate fidelity is one of the highest reported to date in the neutral atom platform [14, 46]; extensive modeling of the two-qubit gate errors (Extended Data Fig. 6 and Methods) suggests that residual unexplained errors are likely the result of imperfect optimization of the time-optimal gate.

We also characterize in more detail the loss during the entangling gates (Fig. 3c). The loss per CZ gate extracted from the slope shows that the probability of correlated loss p_{corr} is orders of magnitude higher than the square of the probability of single-atom loss p_{single}^2 , which represents the expected probability of two-atom loss for uncorrelated single-particle loss. A simulation that assumes all the Rydberg decay leaving the qubit subspace goes to non-interacting states — which, though simpler, is not entirely expected due to blackbody-induced decay to opposite parity states — suggests that most of the correlated loss arises from instances where one atom

decays, interrupts the blockade, and thereby causes the other atom to end up in the Rydberg manifold [56]. The remaining Rydberg state population is then converted to atom loss by the ionization beam. With this mechanism, p_{corr} becomes a similar magnitude to p_{single} . We note that quantitatively characterizing these errors could inform improved decoding in quantum error correction [57] as well as influence achievable code thresholds.

Generation and mapping of two-dimensional Z_2 -ordered GHZ state

The presented qubit mapping and loss detection translate to larger entangled states and many-body dynamics. We use this to prepare Z_2 -ordered GHZ states in the m -qubit manifold. The entanglement is generated with an adiabatic sweep of the many-body Hamiltonian while the atoms are in the r -qubit manifold. We map the entangled state to the non-interacting m -qubit with a similar method described in Fig. 2c. The presence of the long-range interaction beyond the nearest neighbor results in a non-zero energy shift for Z_2 -ordered states. We account for this shift by adding a detuning to the mapping pulse (Extended Data Fig. 9 and Methods). In Fig. 4b, the observed density-density correlation function for the GHZ state of the mapped nuclear spin qubit is presented. The second order correlation function, $g^{(2)}(d_x, d_y)$, is defined as

$$g^{(2)}(d_x, d_y) = \frac{1}{N_{d_x, d_y}} \sum_{i, j: \mathbf{r}_i = \mathbf{r}_j + (d_x, d_y)} \langle n_i n_j \rangle - \langle n_i \rangle \langle n_j \rangle$$

where $\hat{n}_i = |r\rangle_i \langle r|_i$ and N_{d_x, d_y} is the number of the atomic pairs whose position has the relation $\mathbf{r}_i = \mathbf{r}_j + (d_x, d_y)$. To evaluate the GHZ-state preparation fidelity, both population and coherence should be assessed [29]. Our coherence measurement scheme uses global phase rotations as shown in Fig. 4a. We assess the coherence by observing the evolution of the parity value while sweeping the global phase of the $\pi/2$ -pulse (see Extended Data Fig. 9 and Methods).

We use optimal control, based on the Gradient Ascent Pulse Engineering (GRAPE) algorithm, to design a pulse for GHZ-state generation. The system Hamiltonian is written as,

$$H/\hbar = \sum_i \left(\frac{\Omega(t)}{2} \hat{\sigma}_i^X - \Delta(t) \hat{n}_i \right) + \sum_{i < j} \frac{C_6}{|\mathbf{r}_i - \mathbf{r}_j|^6} \hat{n}_i \hat{n}_j$$

where $\hat{\sigma}_i^X = |r\rangle_i \langle m|_i + |m\rangle_i \langle r|_i$ and \mathbf{r}_i is the position of the atoms. The externally controllable global parameters $\Omega(t)$ and $\Delta(t)$ are Rabi frequency and laser detuning relative to the free-space atomic resonance, respectively. We adjust the lattice geometry to homogenize the interactions along each direction of the ladder, which compensates for the measured anisotropic atomic interactions (see Extended Data Fig. 7 and Methods). Unlike previous demonstrations using similar adiabatic schemes [29],

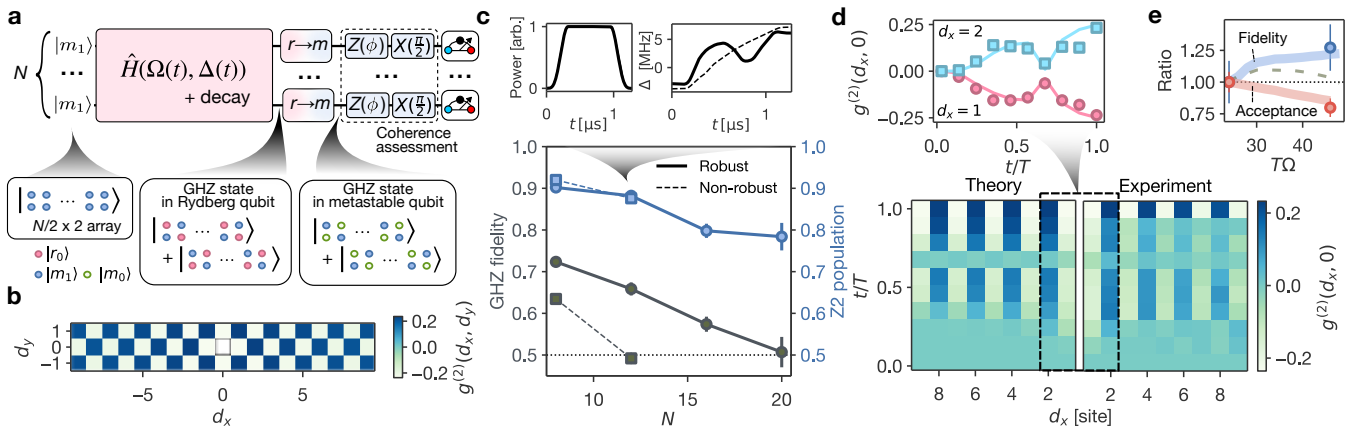


Fig. 4. Disorder-robust generation of Z_2 -ordered GHZ state and mapping to the nuclear spin qubit. **a**, Sequence of mapping and fidelity assessment. After the generation in the Rydberg state manifold, the GHZ state is mapped onto the non-interacting metastable qubit. The coherence is bounded by the phase scan of the global $\pi/2$ -pulse as shown inside the dotted frame. **b**, Observed Z_2 correlation after the qubit mapping. **c**, Scaling behavior of the GHZ-state fidelity in a two-dimensional ladder array after mapping to the m -qubit. Significant improvement is observed with the implementation of a pulse derived from a GRAPE optimization using a cost function considering position fluctuations. For $N = 20$, we observe 78(3)% Z_2 population and measure 51(4)% GHZ-state fidelity. On top, pulse shapes for both robust (solid line) and non-robust (dashed line) pulses for $N = 12$ are presented. **d**, Evolution of the correlation function. (Bottom) Evolution of the d_x direction correlation function, comparing theory and experiment with loss detection. (Top) Comparison of the evolution between theory (solid line) and experiment (dots) at distances $d_x = 1, 2$. **e**, Loss-detected GHZ fidelity and acceptance rate as a function of the total pulse time. The blue dots show the relative change of the GHZ-state fidelity, while the red dots show the relative change of the acceptance rate. The solid lines represent the theory accounting for the loss detection. The dashed line represents the theoretical fidelity with Rydberg decay and without the loss detection, showing a peak due to the trade-off between adiabaticity and decay.

we employ a two-dimensional ladder array. This geometry naturally realizes degenerate ground states of two Z_2 -ordered states when the detuning, Δ , is large, even without local light-shift on the outer edges [29]. However, diagonal interaction introduces sensitivity to fluctuations in the atomic distance. This is because the strength of the diagonal interaction is on the order of $\sim 2\pi \times 1$ MHz, comparable to the typical operating Rabi frequency $2\pi \times 3.0$ MHz of the driving field. By a parameter sweep optimized without accounting for the shot-to-shot fluctuations of the interactions, we observe severe degradation of the GHZ-state coherence and consequently fidelity (Fig. 4c).

To mitigate this effect, the cost function for the GRAPE optimization is modified to explicitly incorporate interaction fluctuations (Methods). Interestingly, the optimized result shows a qualitatively different frequency sweep profile that is non-monotonic with time and crosses the phase transition point, $\Delta_c/\Omega \simeq 1.3$, three times (Extended Data Fig. 8 and Methods). Using this optimized pulse shape, we successfully generate GHZ states with up to 20 atoms.

To elucidate the physics behind this robust protocol, we show the evolution of the correlation function along the ladder direction, $g^{(2)}(d_x, 0)$ in Fig. 4d. A reduction of the correlation is observed in correspondence with the dip in the detuning profile, where the system transitions back into the trivial phase, followed by a revival toward

the end of the pulse as it reenters the ordered phase. The dynamical phase accumulated during the intermediate trivial-phase regime plays a key role in coherently suppressing many-body phase errors induced by atomic position fluctuations, in direct analogy to the spin-echo effect in nuclear magnetic resonance, as further discussed in Ref. [48].

This interference mechanism is generic and can be applied to a broad class of interacting systems where static perturbations break a symmetry of the ideal Hamiltonian. In the present system, the symmetry-breaking perturbation arises from positional fluctuations of the atoms, which break the Z_2 symmetry characterizing the GHZ state. In Ref. [48], we further demonstrate its applicability to GHZ-state generation in quantum Ising models, as well as to Z_3 and Z_4 ordered states and quantum spin liquids in Rydberg arrays.

Detection of the Rydberg decay enables probing many-body dynamics even when there is a significant decay probability. To illustrate this feature, we compare the loss-detected fidelity of the GHZ states generated using two pulses, each with a different total pulse length. As the total pulse time, T , increases, we observe a trade-off: While the acceptance rate decreases as a result of increased Rydberg decay, the GHZ-state fidelity achieved improves. The enhancement results from a more adiabatic evolution of the longer pulse. Unlike the experiment on Fig. 2e, the non-Hermitian contribution from Ryd-

berg decay does not significantly affect the many-body dynamics, as its energy scale remains small compared to the energy scales of the Hamiltonian (see Extended Data Fig. 10 and Methods). In this regime, and at the expense of statistics, the loss-detected system evolves indistinguishably to a system with a Rydberg lifetime of 1.2(2) ms, a similar timescale to circular Rydberg states [58, 59].

Outlook

This architecture can be extended in several directions. The versatility of digital circuits incorporating non-local connectivity can be used for optimization of sensors such as programmable optical clocks [20, 25], featuring error correction in state preparation, state read out (signal “decoding”), or even during sensor operation [39], where all stages besides sensing occur in the robust nuclear qubit while sensing arises after mapping to the optical qubit [16, 22, 23, 60]. Such circuits could also be combined with stroboscopic shelving of optical coherence into the nuclear qubit for mid-circuit measurements on an atomic clock, to enable adaptive feedback.

At the same time, the mapping of Rydberg qubits to computational qubits allows for coherent atom rearrangement [18] — otherwise precluded by the Rydberg lifetime — enabling direct access to entanglement witnesses of quantum criticality and topological order [61, 62]. Meanwhile, this mapping allows analog quantum simulations to be leveraged for generating resource states for quantum computation [63, 64] and quantum metrol-

ogy [21, 65]. Conversely, mapping the computational qubit to the Rydberg qubit allows programmable entangled state preparation for subsequent many-body evolution.

The high-fidelity decay detection enabled by our approach opens significant opportunities for both quantum simulation and quantum computing. When the Rydberg decay rate is larger than the characteristic energy scales of the Hamiltonian, the capability to isolate no-decay events can reveal exotic phenomena such as entanglement propagation beyond the Lieb-Robinson bound [66, 67]. On the other hand, when the decay rate is smaller, we numerically find that the system behaves indistinguishably from the unitary evolution after post-selection. The achieved effective Rydberg lifetime could enable Rydberg based quantum simulations with unprecedented evolution time. Moreover, high-fidelity control of the Rydberg transition via loss-detected error mitigation is particularly intriguing, as it eases the requirements for optical power and may contribute to scalable two-qubit gate implementation for neutral-atom quantum computers.

Finally, the use of GRAPE in many-body systems has enabled the discovery of a robust, experiment-tailored protocol that departs significantly from conventional monotonic adiabatic ramps. These results highlight the potential of optimal control techniques to uncover efficient strategies for steering strongly interacting systems and are expected to drive further advances in analog quantum simulation of many-body systems. For example, studies of quantum spin liquids [5] might be advanced by combining robust sweep protocols [48] with the error detection schemes reported here.

-
- [1] M. Saffman, Quantum computing with atomic qubits and Rydberg interactions: Progress and challenges, *J. Phys. B* **49**, 202001 (2016).
 - [2] D. Bluvstein, S. J. Evered, A. A. Geim, S. H. Li, H. Zhou, T. Manovitz, S. Ebadi, M. Cain, M. Kalinowski, D. Hangleiter, *et al.*, Logical quantum processor based on reconfigurable atom arrays, *Nature* **626**, 58 (2024).
 - [3] T. Graham, Y. Song, J. Scott, C. Poole, L. Phuttitarn, K. Jooya, P. Eichler, X. Jiang, A. Marra, B. Grinkemeyer, *et al.*, Multi-qubit entanglement and algorithms on a neutral-atom quantum computer, *Nature (London)* **604**, 457 (2022).
 - [4] A. Browaeys and T. Lahaye, Many-body physics with individually controlled Rydberg atoms, *Nature Physics* **16**, 132 (2020).
 - [5] G. Semeghini, H. Levine, A. Keesling, S. Ebadi, T. T. Wang, D. Bluvstein, R. Verresen, H. Pichler, M. Kalinowski, R. Samajdar, *et al.*, Probing topological spin liquids on a programmable quantum simulator, *Science* **374**, 1242 (2021).
 - [6] A. L. Shaw, Z. Chen, J. Choi, D. K. Mark, P. Scholl, R. Finkelstein, A. Elben, S. Choi, and M. Endres, Benchmarking highly entangled states on a 60-atom analogue quantum simulator, *Nature* **628**, 71 (2024).
 - [7] M. A. Norcia, A. W. Young, W. J. Eckner, E. Oelker, J. Ye, and A. M. Kaufman, Seconds-scale coherence on an optical clock transition in a tweezer array, *Science* **366**, 93 (2019).
 - [8] I. S. Madjarov, A. Cooper, A. L. Shaw, J. P. Covey, V. Schkolnik, T. H. Yoon, J. R. Williams, and M. Endres, An atomic-array optical clock with single-atom readout, *Phys. Rev. X* **9**, 041052 (2019).
 - [9] A. W. Young, W. J. Eckner, W. R. Milner, D. Kedar, M. A. Norcia, E. Oelker, N. Schine, J. Ye, and A. M. Kaufman, Half-minute-scale atomic coherence and high relative stability in a tweezer clock, *Nature (London)* **588**, 408 (2020).
 - [10] A. Jenkins, J. W. Lis, A. Senoo, W. F. McGrew, and A. M. Kaufman, Ytterbium nuclear-spin qubits in an optical tweezer array, *Phys. Rev. X* **12**, 021027 (2022).
 - [11] S. Ma, A. P. Burgers, G. Liu, J. Wilson, B. Zhang, and J. D. Thompson, Universal gate operations on nuclear spin qubits in an optical tweezer array of ^{171}Yb atoms, *Phys. Rev. X* **12**, 021028 (2022).
 - [12] S. Ma, G. Liu, P. Peng, B. Zhang, S. Jandura, J. Claes, A. P. Burgers, G. Pupillo, S. Puri, and J. D. Thompson, High-fidelity gates and mid-circuit erasure conversion in an atomic qubit, *Nature* **622**, 279 (2023).

- [13] J. W. Lis, A. Senoo, W. F. McGrew, F. Rönchen, A. Jenkins, and A. M. Kaufman, Midcircuit operations using the omg architecture in neutral atom arrays, *Physical Review X* **13**, 041035 (2023).
- [14] J. Muniz, M. Stone, D. Stack, M. Jaffe, J. Kindem, L. Wadleigh, E. Zalus-Geller, X. Zhang, C.-A. Chen, M. Norcia, *et al.*, High-fidelity universal gates in the 171 Yb ground-state nuclear-spin qubit, *PRX Quantum* **6**, 020334 (2025).
- [15] A. D. Ludlow, M. M. Boyd, J. Ye, E. Peik, and P. O. Schmidt, Optical atomic clocks, *Rev. Mod. Phys.* **87**, 637 (2015).
- [16] L. Pezze, A. Smerzi, M. K. Oberthaler, R. Schmied, and P. Treutlein, Quantum metrology with nonclassical states of atomic ensembles, *Reviews of Modern Physics* **90**, 035005 (2018).
- [17] T. I. Andersen, N. Astrakhantsev, A. H. Karamlou, J. Berndtsson, J. Motruk, A. Szasz, J. A. Gross, A. Schuckert, T. Westerhout, Y. Zhang, *et al.*, Thermalization and criticality on an analogue–digital quantum simulator, *Nature* **638**, 79 (2025).
- [18] D. Bluvstein, H. Levine, G. Semeghini, T. T. Wang, S. Ebadi, M. Kalinowski, A. Keesling, N. Maskara, H. Pichler, M. Greiner, *et al.*, A quantum processor based on coherent transport of entangled atom arrays, *Nature (London)* **604**, 451 (2022).
- [19] H.-Y. Huang, M. Broughton, J. Cotler, S. Chen, J. Li, M. Mohseni, H. Neven, R. Babbush, R. Kueng, J. Preskill, *et al.*, Quantum advantage in learning from experiments, *Science* **376**, 1182 (2022).
- [20] R. Finkelstein, R. B.-S. Tsai, X. Sun, P. Scholl, S. Direkci, T. Gefen, J. Choi, A. L. Shaw, and M. Endres, Universal quantum operations and ancilla-based read-out for tweezer clocks, *Nature* **634**, 321 (2024).
- [21] W. J. Eckner, N. D. Oppong, A. Cao, A. W. Young, W. R. Milner, J. M. Robinson, J. Ye, and A. M. Kaufman, Realizing spin squeezing with Rydberg interactions in a programmable optical clock, *Nature (London)* **621**, 734 (2023).
- [22] C. D. Marciniak, T. Feldker, I. Pogorelov, R. Kaubruegger, D. V. Vasilyev, R. van Bijnen, P. Schindler, P. Zoller, R. Blatt, and T. Monz, Optimal metrology with programmable quantum sensors, *Nature* **603**, 604 (2022).
- [23] E. Pedrozo-Peñafiel, S. Colombo, C. Shu, A. F. Adiyatullin, Z. Li, E. Mendez, B. Braverman, A. Kawasaki, D. Akamatsu, Y. Xiao, *et al.*, Entanglement on an optical atomic-clock transition, *Nature* **588**, 414 (2020).
- [24] N. Schine, A. W. Young, W. J. Eckner, M. J. Martin, and A. M. Kaufman, Long-lived bell states in an array of optical clock qubits, *Nature Physics* **18**, 1067 (2022).
- [25] A. Cao, W. J. Eckner, T. Lukin Yelin, A. W. Young, S. Jandura, L. Yan, K. Kim, G. Pupillo, J. Ye, N. Darkwah Oppong, *et al.*, Multi-qubit gates and schrödinger cat states in an optical clock, *Nature* **634**, 315 (2024).
- [26] K. Barnes, P. Battaglino, B. J. Bloom, K. Cassella, R. Coxe, N. Crisosto, J. P. King, S. S. Kondov, K. Kotru, S. C. Larsen, *et al.*, Assembly and coherent control of a register of nuclear spin qubits, *Nat. Commun.* **13**, 2779 (2022).
- [27] H. Levine, A. Keesling, A. Omran, H. Bernien, S. Schwartz, A. S. Zibrov, M. Endres, M. Greiner, V. Vuletić, and M. D. Lukin, High-fidelity control and entanglement of Rydberg-atom qubits, *Physical review letters* **121**, 123603 (2018).
- [28] I. S. Madjarov, J. P. Covey, A. L. Shaw, J. Choi, A. Kale, A. Cooper, H. Pichler, V. Schkolnik, J. R. Williams, and M. Endres, High-fidelity entanglement and detection of alkaline-earth Rydberg atoms, *Nat. Phys.* **16**, 857 (2020).
- [29] A. Omran, H. Levine, A. Keesling, G. Semeghini, T. T. Wang, S. Ebadi, H. Bernien, A. S. Zibrov, H. Pichler, S. Choi, *et al.*, Generation and manipulation of Schrödinger cat states in Rydberg atom arrays, *Science* **365**, 570 (2019).
- [30] A. Radnaev, W. Chung, D. Cole, D. Mason, T. Balance, M. Bedalov, D. Belknap, M. Berman, M. Blakely, I. Bloomfield, *et al.*, Universal neutral-atom quantum computer with individual optical addressing and nondestructive readout, *PRX Quantum* **6**, 030334 (2025).
- [31] M. Kjaergaard, M. E. Schwartz, J. Braumüller, P. Krantz, J. I.-J. Wang, S. Gustavsson, and W. D. Oliver, Superconducting qubits: Current state of play, *Annu. Rev. Condens. Matter Phys.* **11**, 369 (2020).
- [32] C. D. Bruzewicz, J. Chiaverini, R. McConnell, and J. M. Sage, Trapped-ion quantum computing: Progress and challenges, *Appl. Phys. Rev.* **6**, 021314 (2019).
- [33] L. Henriët, L. Beguin, A. Signoles, T. Lahaye, A. Browaeys, G.-O. Reymond, and C. Jurczak, Quantum computing with neutral atoms, *Quantum* **4**, 327 (2020).
- [34] G. Q. Ai *et al.*, Quantum error correction below the surface code threshold, *Nature* **638**, 920 (2024).
- [35] I. M. Georgescu, S. Ashhab, and F. Nori, Quantum simulation, *Reviews of Modern Physics* **86**, 153 (2014).
- [36] A. J. Daley, I. Bloch, C. Kokail, S. Flannigan, N. Pearson, M. Troyer, and P. Zoller, Practical quantum advantage in quantum simulation, *Nature* **607**, 667 (2022).
- [37] L. Lamata, A. Parra-Rodriguez, M. Sanz, and E. Solano, Digital-analog quantum simulations with superconducting circuits, *Advances in Physics: X* **3**, 1457981 (2018).
- [38] R. Kaubruegger, A. Shankar, D. V. Vasilyev, and P. Zoller, Optimal and variational multiparameter quantum metrology and vector-field sensing, *PRX Quantum* **4**, 020333 (2023).
- [39] S. Zhou, M. Zhang, J. Preskill, and L. Jiang, Achieving the heisenberg limit in quantum metrology using quantum error correction, *Nature communications* **9**, 78 (2018).
- [40] T. Kielinski, P. O. Schmidt, and K. Hammerer, GHZ protocols enhance frequency metrology despite spontaneous decay, *Science Advances* **10**, eadr1439 (2024).
- [41] S. J. Evered, M. Kalinowski, A. A. Geim, T. Manovitz, D. Bluvstein, S. H. Li, N. Maskara, H. Zhou, S. Ebadi, M. Xu, *et al.*, Probing the kitaev honeycomb model on a neutral-atom quantum computer, *Nature* **645**, 341 (2025).
- [42] B. W. Reichardt, A. Paetznick, D. Aasen, I. Basov, J. M. Bello-Rivas, P. Bonderson, R. Chao, W. van Dam, M. B. Hastings, A. Paz, *et al.*, Logical computation demonstrated with a neutral atom quantum processor, *arXiv preprint arXiv:2411.11822* (2024).
- [43] R. Chinnarasu, C. Poole, L. Phuttitarn, A. Noori, T. Graham, S. Coppersmith, A. Balantekin, and M. Saffman, Variational simulation of the lipkin-meshkov-glick model on a neutral atom quantum computer, *PRX Quantum* **6**, 020350 (2025).
- [44] M. Norcia, W. Cairncross, K. Barnes, P. Battaglino, A. Brown, M. Brown, K. Cassella, C.-A. Chen, R. Coxe, D. Crow, *et al.*, Midcircuit qubit measurement and rearrangement in a Yb 171 atomic array, *Physical Review X*

- 13**, 041034 (2023).
- [45] P. Scholl, A. L. Shaw, R. B.-S. Tsai, R. Finkelstein, J. Choi, and M. Endres, Erasure conversion in a high-fidelity Rydberg quantum simulator, *Nature* **622**, 273 (2023).
- [46] R. B.-S. Tsai, X. Sun, A. L. Shaw, R. Finkelstein, and M. Endres, Benchmarking and fidelity response theory of high-fidelity Rydberg entangling gates, *PRX Quantum* **6**, 010331 (2025).
- [47] M. Peper, Y. Li, D. Y. Knapp, M. Bileska, S. Ma, G. Liu, P. Peng, B. Zhang, S. P. Horvath, A. P. Burgers, *et al.*, Spectroscopy and modeling of Yb 171 Rydberg states for high-fidelity two-qubit gates, *Physical Review X* **15**, 011009 (2025).
- [48] Z. Zeng, G. Giudici, A. Senoo, A. Baumgärtner, A. M. Kaufman, and H. Pichler, Adiabatic echo protocols for robust quantum many-body state preparation, arXiv preprint arXiv:2506.12138 (2025).
- [49] S. J. Glaser, U. Boscain, T. Calarco, C. P. Koch, W. Köckenberger, R. Kosloff, I. Kuprov, B. Luy, S. Schirmer, T. Schulte-Herbrüggen, D. Sugny, and F. K. Wilhelm, Training Schrödinger’s cat: quantum optimal control. Strategic report on current status, visions and goals for research in Europe, *European Physical Journal D* **69**, 279 (2015).
- [50] E. Deist, Y.-H. Lu, J. Ho, M. K. Pasha, J. Zeiher, Z. Yan, and D. M. Stamper-Kurn, Mid-circuit cavity measurement in a neutral atom array, *Phys. Rev. Lett.* **129**, 203602 (2022).
- [51] W. Huie, L. Li, N. Chen, X. Hu, Z. Jia, W. K. C. Sun, and J. P. Covey, Repetitive readout and real-time control of nuclear spin qubits in ^{171}Yb atoms, *PRX Quantum* **4**, 030337 (2023).
- [52] B. Hu, J. Sinclair, E. Bytyqi, M. Chong, A. Rudelis, J. Ramette, Z. Vendeiro, and V. Vuletić, Site-selective cavity readout and classical error correction of a 5-bit atomic register, *Physical Review Letters* **134**, 120801 (2025).
- [53] K. Mølmer, Y. Castin, and J. Dalibard, Monte carlo wave-function method in quantum optics, *Journal of the Optical Society of America B* **10**, 524 (1993).
- [54] S. Jandura and G. Pupillo, Time-optimal two- and three-qubit gates for Rydberg atoms, *Quantum* **6**, 712 (2022).
- [55] S. J. Evered, D. Bluvstein, M. Kalinowski, S. Ebadi, T. Manovitz, H. Zhou, S. H. Li, A. A. Geim, T. T. Wang, N. Maskara, *et al.*, High-fidelity parallel entangling gates on a neutral-atom quantum computer, *Nature* **622**, 268 (2023).
- [56] Y. Wu, S. Kolkowitz, S. Puri, and J. D. Thompson, Erasure conversion for fault-tolerant quantum computing in alkaline earth Rydberg atom arrays, *Nat. Commun.* **13**, 4657 (2022).
- [57] G. Baranes, M. Cain, J. Ataiades, D. Bluvstein, J. Sinclair, V. Vuletic, H. Zhou, and M. D. Lukin, Leveraging atom loss errors in fault tolerant quantum algorithms, arXiv preprint arXiv:2502.20558 (2025).
- [58] M. Saffman, T. G. Walker, and K. Mølmer, Quantum information with Rydberg atoms, *Reviews of modern physics* **82**, 2313 (2010).
- [59] H. Wu, R. Richaud, J.-M. Raimond, M. Brune, and S. Gleyzes, Millisecond-lived circular Rydberg atoms in a room-temperature experiment, *Physical Review Letters* **130**, 023202 (2023).
- [60] R. Kaubruegger, D. V. Vasilyev, M. Schulte, K. Hammerer, and P. Zoller, Quantum variational optimization of Ramsey interferometry and atomic clocks, *Phys. Rev. X* **11**, 041045 (2021).
- [61] H. Pichler, G. Zhu, A. Seif, P. Zoller, and M. Hafezi, Measurement protocol for the entanglement spectrum of cold atoms, *Phys. Rev. X* **6**, 041033 (2016).
- [62] R. Ott, T. V. Zache, N. Maskara, M. D. Lukin, P. Zoller, and H. Pichler, Probing topological entanglement on large scales, *Physical Review Letters* **135**, 090401 (2025).
- [63] A. Martin, L. Lamata, E. Solano, and M. Sanz, Digital-analog quantum algorithm for the quantum Fourier transform, *Physical Review Research* **2**, 013012 (2020).
- [64] B. Bauer, S. Bravyi, M. Motta, and G. K.-L. Chan, Quantum algorithms for quantum chemistry and quantum materials science, *Chemical reviews* **120**, 12685 (2020).
- [65] G. Bornet, G. Emperauger, C. Chen, B. Ye, M. Block, M. Bintz, J. A. Boyd, D. Barredo, T. Comparin, F. Mezzacapo, *et al.*, Scalable spin squeezing in a dipolar Rydberg atom array, *Nature* **621**, 728 (2023).
- [66] Y. Zhang, J. Carrasquilla, and Y. B. Kim, Observation of a non-hermitian supersonic mode on a trapped-ion quantum computer, *Nature Communications* **16**, 3286 (2025).
- [67] C.-M. Halati, A. Sheikhan, G. Morigi, C. Kollath, and S. B. Jäger, From light-cone to supersonic propagation of correlations by competing short- and long-range couplings, arXiv preprint arXiv:2503.13306 (2025).
- [68] W. Tian, W. J. Wee, A. Qu, B. J. M. Lim, P. R. Datla, V. P. W. Koh, and H. Loh, Parallel assembly of arbitrary defect-free atom arrays with a multitweezer algorithm, *Physical Review Applied* **19**, 034048 (2023).
- [69] T. O. Höhn, E. Staub, G. Brochier, N. Darkwah Oppong, and M. Aidelburger, State-dependent potentials for the $s\ 0\ 1$ and $p\ 0\ 3$ clock states of neutral ytterbium atoms, *Physical Review A* **108**, 053325 (2023).
- [70] L. Su, A. Douglas, M. Szurek, A. H. Hébert, A. Krahn, R. Groth, G. A. Phelps, O. Marković, and M. Greiner, Fast single atom imaging for optical lattice arrays, *Nature Communications* **16**, 1017 (2025).
- [71] M. Miranda, R. Inoue, Y. Okuyama, A. Nakamoto, and M. Kozuma, Site-resolved imaging of ytterbium atoms in a two-dimensional optical lattice, *Physical Review A* **91**, 063414 (2015).
- [72] A. C. Wilson, C. Ospelkaus, A. VanDevender, J. A. Mlynek, K. R. Brown, D. Leibfried, and D. J. Wineland, A 750-mW, continuous-wave, solid-state laser source at 313 nm for cooling and manipulating trapped $^9\text{Be}^+$ ions, *Applied Physics B* **105**, 741 (2011).
- [73] N. Lorenz, *A Rydberg tweezer platform with potassium atoms*, Ph.D. thesis, lmu (2021).
- [74] C. D. Marciniak, *Design and operation of a Penning ion trap for quantum simulation*, Ph.D. thesis (2019).
- [75] A. P. Burgers, S. Ma, S. Saskin, J. Wilson, M. A. Alarcón, C. H. Greene, and J. D. Thompson, Controlling Rydberg excitations using ion-core transitions in alkaline-earth atom-tweezer arrays, *PRX Quantum* **3**, 020326 (2022).
- [76] A. L. Shaw, *Learning, Verifying, and Erasing Errors on a Chaotic and Highly Entangled Programmable Quantum Simulator*, Ph.D. thesis, California Institute of Technology, Pasadena, California (2024), defended April 11, 2024.
- [77] T. Wilk, A. Gaëtan, C. Evellin, J. Wolters, Y. Miroshnychenko, P. Grangier, and A. Browaeys, Entanglement of two individual neutral atoms using Rydberg blockade,

[Phys. Rev. Lett.](#) **104**, 010502 (2010).

- [78] N. Khaneja, T. Reiss, C. Kehlet, T. Schulte-Herbrüggen, and S. J. Glaser, Optimal control of coupled spin dynamics: design of NMR pulse sequences by gradient ascent algorithms, [Journal of Magnetic Resonance](#) **172**, 296 (2005).
- [79] B. Zhang, G. Liu, G. Bornet, S. P. Horvath, P. Peng, S. Ma, S. Huang, S. Puri, and J. D. Thompson, Leveraging erasure errors in logical qubits with metastable ^{171}Yb atoms, [arXiv preprint arXiv:2506.13724](#) (2025).

METHODS

Resource efficient atom preparation

The total number of optical tweezers that can be generated is limited by available laser power. Further, without additional steps, only about $\sim 50\%$ of these tweezers are occupied due to the stochastic nature of the loading process. To improve on this inefficiency and prepare fully occupied, defect-free arrays, we combine enhanced loading with rearrangement.

^{171}Yb is loaded from the 556 nm narrow-line magneto-optical trap (MOT) to the 532 nm tweezer array generated by acousto-optic deflectors (AOD) in a crossed configuration. Using the enhanced loading method reported in previous work [10], we load single atoms with a $\sim 90\%$ probability. For the non-destructive imaging [13], atoms are transferred to the 767 nm tweezer array generated by a liquid crystal spatial light modulator (SLM). Unlike previous experiments that used the 759 nm clock magic wavelength [15], we employ 767 nm tweezer during detections and coherent manipulations.

After imaging, the atoms are rearranged by moving 532 nm tweezers, using row-by-row compression. The resulting loading and rearrangement efficiency is shown in Extended Data Fig. 1d. By combining rearrangement and enhanced loading [68], we achieve $> 50\%$ defect-free array sorting success of up to $> 60\%$ atoms to the total tweezer array, such as a 40 atom ladder out of a 64-tweezer loading array. Remarkably, even for a 50 atom array sorted out of 64 total tweezers, we get a $> 20\%$ success rate. The performance of this sorting technique is summarized in Extended Data Fig. 1.

Preparation of qubits in the metastable manifold

Our state preparation protocol builds on methods developed in previous work [13]. After loading and sorting the atoms, we apply Raman sideband cooling to bring them to the motional ground state in the radial directions (i.e., directions transverse to the tweezer propagation direction). Using sideband spectroscopy, we verify cooling to an average occupation number $\bar{n} < 0.05$.

In the axial direction, the atoms are cooled only via gray molasses, as both the clock and Rydberg laser beams are applied transversely and do not couple strongly to axial motion. After Raman sideband cooling and optical pumping, we rotate the quantization magnetic field perpendicular to the initial magnetic field.

To prepare the desired spin state, we perform a spin flip from $m_F = +1/2$ to $m_F = -1/2$ in the ground-state manifold via a Raman rotation, followed by a σ^+ -polarized clock pulse that excites the atom to the metastable clock state [10]. Importantly, we implement a state-preparation erasure protocol by applying resonant light onto the $^1\text{S}_0 \rightarrow ^1\text{P}_1$ transition: Any error in the spin flip or clock excitation results in resonant scattering

(preparation erasure) and atom loss (delayed erasure), allowing us to herald successful state preparation.

To ensure that the motional ground state is preserved during the clock excitation, we employ a motional-state-preserving pulse (MPP), as demonstrated in Ref. [13]. Using release-and-recapture thermometry on both ground and metastable states, we confirm that this excitation process introduces negligible heating (see Extended Data Fig. 1g).

Motional state preserving pulse (MPP) in non-magic tweezer

While 759 nm is the exact magic wavelength for the clock transition, generating high optical power at this wavelength is challenging and typically requires Ti:sapphire laser systems. For scalable architectures, operation at wavelengths accessible with fiber-laser technology is therefore preferable.

In our current tweezer system, operating at 767 nm generated by a frequency-doubled Er-doped fiber amplifier, we experimentally confirm performance comparable to that at the exact magic wavelength. This includes high-contrast σ -qubit Rabi oscillations with over > 60 coherent cycles [13].

To evaluate the feasibility of MPP pulses across a broader range of wavelengths, we theoretically analyze their fidelity under varying levels of differential light shift inhomogeneity. We find that, provided the tweezer-induced light shifts remain sufficiently uniform across the atomic array, MPP pulses retain high fidelity even away from the exact magic wavelength.

Our simulation assumes a one-dimensional harmonic oscillator Hamiltonian

$$H_{\text{total}} = H_{\text{diag}} + H_{\text{light}}.$$

After the rotating wave approximation, the diagonal part, H_{diag} , consists of the energy levels of the harmonic oscillator states, as well as the laser detuning, Δ_m , coming from the spatially varying differential light shifts due to the inhomogeneity of the traps:

$$H_{\text{diag}} = \sum_i \omega_g i |g, i\rangle \langle g, i| + \sum_j (\omega_m j + \Delta_m) |m, j\rangle \langle m, j|,$$

where i, j are the labels for the motional levels. Here, it is assumed that the ground state, g , and the metastable clock state, m , have different trap frequencies ω_g and ω_m .

The optical excitation term is given by H_{light} , where

$$H_{\text{light}} = \sum_{i,j} \Omega_m \langle i |_{\omega_m} e^{ikx} |j\rangle_{\omega_g} |m, i\rangle \langle g, j| + \text{h.c.}$$

The motional state matrix element for the non-magic condition is explicitly written as

$$\langle i |_{\omega_m} e^{ikx} |j\rangle_{\omega_g} = \int_{-\infty}^{\infty} dx \psi_i(x, \omega_m)^* e^{ikx} \psi_j(x, \omega_g),$$

where $\psi_i(x, \omega)$ are the eigenstates of the one-dimensional harmonic oscillator with trap frequency ω .

Using the polarizability data of ^{171}Yb [69], we numerically simulate this Hamiltonian, including up to the 15th motional level as shown in the Extended Data Fig. 1g. The largest error contribution stems from the detuning caused by the tweezer inhomogeneity, and in the absence of inhomogeneity, the performance of the MPP is not significantly degraded by non-magic traps.

Fast destructive imaging and three outcome measurements

For spin measurements as well as erasure detection, we employ destructive imaging using alternating counter-propagating beams resonant to the $^1\text{S}_0 \longleftrightarrow ^1\text{P}_1$ transition, closely following the method demonstrated in [70]. We alternate the two beams with a frequency of 3 MHz. For erasure detection, imaging is performed in 250 kHz-deep tweezers used for clock and qubit operations, where the depth is quoted for the trapping potential of the ground state.

By selecting a sufficiently large region of interest (ROI) for each atom, we achieve clear separation between camera background counts and the single-atom fluorescence peak in photon counting histograms (Extended Data Fig. 2c). A fit to two Gaussians indicates an erasure infidelity of $< 0.5\%$, after renormalizing the height to equalize the areas of the two peaks.

For spin detection in dense tweezer arrays, imaging in shallow tweezers leads to fast atomic diffusion, causing fluorescence to leak into the ROIs of neighboring tweezers and degrade spin state discrimination. To pin the atoms in place, we apply 9.6 MHz-deep tweezers (Extended Data Fig. 2d). Because the excited state $^1\text{P}_1$ is also trapped at 767 nm (Extended Data Fig. 1c), this creates a deep confining potential even while the atoms scatter 399 nm photons at high rates [71]. Using this approach, we achieve an infidelity of $< 0.2\%$, while still using individual ROI sizes smaller than half the tweezer spacing.

We can optimize the imaging time to minimize infidelity in dense arrays. We interpret this as a compromise between collecting sufficient fluorescence and minimizing cross-talk from neighboring atoms. As shown in Extended Data Fig. 2e, we find an optimal imaging time near $15 \mu\text{s}$. We note here that due to daily fluctuations in beam balancing and intensity, the ideal imaging time fluctuates and some datasets were measured with a time of $17 \mu\text{s}$.

Although the fast imaging itself takes only 15–17 μs , the current total time for the three-outcome measurement is limited by the camera exposure, which is currently set by the duration of the initial non-destructive images. This could be improved in future iterations via software-controlled variable exposure. In that case, the limiting factor would become the tweezer ramp-up time

prior to imaging, which is 0.5 ms. While the destructive imaging is largely insensitive to atomic temperature, loss during the ramp imposes a constraint on overall imaging speed. Nevertheless, we project a total readout time below 3 ms for the full three-outcome sequence.

Loss and Error Budget of the Three-Outcome Measurement

Extended Data Table I presents the detection probabilities for each outcome of the three-outcome spin measurement. Each row corresponds to a different prepared qubit state, with the columns indicating: correct detections (diagonal), spin mislabeling errors (off-diagonal), and atom loss (rightmost column). While preparation erasure detection is applied, no correction is made for spin-flip errors introduced during the preparation of each input state.

The loss and infidelity observed in Table I arise from two main sources: (1) errors during state preparation, and (2) errors introduced during the readout sequence. Table II details the preparation error budget, listing for each step: (i) the atom loss probability, (ii) whether the error is detectable via erasure, and (iii) any associated spin-flip error. Most preparation-related loss arises from imaging and the tweezer ramp-down used for *o*-qubit operations. Spin-flip errors primarily result from polarization imperfections during the transfer into the metastable manifold, and from the π -pulse in the metastable manifold used to prepare $|m_0\rangle$. The total state preparation loss is 2.1(2)% for $|m_1\rangle$ and 2.7(2)% for $|m_0\rangle$, which reduce to 0.8(1)% and 1.2(2)%, respectively, after erasure correction.

Following state preparation, the three-outcome measurement sequence introduces additional sources of atom loss and spin mislabeling—defined as the incorrect assignment of a spin state (see Table III). De-excitation from the clock state is performed using fast π -pulses in free space. The dominant contribution arises from detuning errors caused by tweezer-induced light shifts (when operating in free space) and clock-light-induced shifts (from changing drive strengths throughout the sequence). These can, in principle, be mitigated by dynamically adjusting the laser frequency.

Spin mislabeling is primarily caused by spurious π -polarized components in the clock beam, which can drive unwanted transitions from $|m_0\rangle$ to $|g_0\rangle$. These polarization impurities may stem from imperfections in the optical beam or from misalignment of the magnetic field direction.

Destructive imaging is performed in deep tweezers, where the associated ramp-up of the tweezer potential induces additional Raman scattering. Other sources of error include imperfect spin rotations in the metastable manifold during state mapping and a finite probability of failing to identify an atom during imaging. Table III distinguishes between loss and spin-mislabeling errors,

and also indicates whether each error affects the first or second spin readout. Due to the sequential nature of the detection, some errors—particularly those affecting atoms in $|m_0\rangle$ —are encountered twice, amplifying their impact.

While the spin mislabeling errors inferred from Table III are in good agreement with the measured spin infidelities in Table I, we observe a clear discrepancy in the total atom loss probability. This suggests the presence of an uncharacterized loss mechanism. Based on the larger discrepancy observed for the second spin readout $|m_0\rangle$, we hypothesize that the loss originates from the final ramp-up of the tweezer potential immediately preceding destructive imaging—a step encountered twice by $|m_0\rangle$ atoms and not fully captured in individual calibration measurements we operated. Further investigation of this loss channel is left for future work.

Single-qubit operation in the metastable nuclear qubit

Our single-qubit gate is operated with two different detunings depending on the applications. For the qubit mapping experiment, we choose a laser frequency positioned between the hyperfine lines of the excited 3D_1 state to enable fast qubit rotations relative to the Rydberg dephasing rate. Under this condition, a Rabi frequency of $2\pi \times 2.9$ MHz is achieved due to constructive interference between the two Raman pathways.

For the two-qubit gate experiment, we use a slower Rabi frequency with an intermediate state detuning of approximately $-2\pi \times 2$ GHz from the $F = 3/2$ transition to reduce both scattering from the intermediate state and errors associated with the finite turn-on time of the AOM across multiple pulses.

Single-qubit Clifford operations include a Z gate implemented via phase tracking, taking advantage of the qubit energy splitting $2\pi \times 9.5$ kHz. Since this implementation is free from scattering error, the total scattering-induced error per Clifford gate is reduced relative to previous work [13].

To assess the fidelity of our single-qubit operations, we perform randomized benchmarking (RB) using single-qubit Clifford sequences, as shown in Extended Data Fig. 3c. For benchmarking the gates, we compare both erasure detection and loss detection schemes. As shown in Ref. [13], scattering to the 3P_1 state (which decays to the 1S_0 state) dominates the error mechanism in this method. Consequently, we observe improvements of similar magnitude using either erasure or loss detection.

The RB data are fit using the model $ap^l + b$, where a and p are fit parameters and l is the number of gates. In the plot shown in Extended Data Fig. 3, we assume $b = 0$ for the case without loss detection, and $b = 1/2$ for the case with loss detection. The gate infidelity is then extracted as $(1 - b)(1 - p)$.

Since the Z -gate is free from the scattering, we at-

tribute most of the error to the X -gate where in our sequence we have 1.6 of $\pi/2$ -pulses on average per single-qubit Clifford gate.

Measurement error correction for the Bell state

Based on the characterization of the preparation and measurement errors, we can estimate the true Bell state fidelity [29]. We define the measurement matrix

$$M = \begin{pmatrix} 1 - \epsilon_{00} & \epsilon_{10} \\ \epsilon_{01} & 1 - \epsilon_{11} \end{pmatrix}$$

for the measurement of a single spin, such that the relation between the measured count of each spin, (N'_0, N'_1) , and the actual count free from the measurement error, (N_0, N_1) , is

$$\begin{pmatrix} N'_0 \\ N'_1 \end{pmatrix} = M \begin{pmatrix} N_0 \\ N_1 \end{pmatrix},$$

Here, we are not assuming conservation of counts such as $\epsilon_{00} = \epsilon_{01}$ since our measurement also induces loss.

To correct for measurement error, we can infer the actual counts (N_0, N_1) from the measured count (N'_0, N'_1) by solving

$$\min_{N_0, N_1} \left\| \begin{pmatrix} N'_0 \\ N'_1 \end{pmatrix} - M \begin{pmatrix} N_0 \\ N_1 \end{pmatrix} \right\|$$

In the two-qubit experiments, we use $M \otimes M$ as a measurement matrix. Using this method, we analyze the metastable state Bell state data in Fig. 1. The measurement error corrected metastable Bell state fidelity is 99.0(3)%. The discrepancy to the two-qubit gate error is likely due to the loss-detected infidelity of single-qubit gate as well as $|m_1\rangle$ preparation infidelity.

We note that the dominant measurement error from the loss detectable measurement is not caused by the imbalanced detection probability, ϵ_{00} , ϵ_{11} , of each spin but rather by the spin mislabeling errors in the detection, ϵ_{01} , ϵ_{10} . Indeed, if we assume $\epsilon_{10} = 0$, $\epsilon_{01} = 0$ in the analysis above, the corrected Bell fidelity is 98.7(3)%, very similar to the value before the correction, 98.6(3)%.

UV system and T_2^* coherence of the Rydberg qubit

For coherent manipulation of the 302 nm single-photon transition to the Rydberg state, we use a laser system based on sum-frequency generation (SFG) and second-harmonic generation (SHG) [24, 72]. An overview of the system is shown in Extended Data Fig. 4a.

The 977 nm light is generated by a home-built interference filter diode laser (IFDL), which is locked to an ultra-low expansion (ULE) cavity with finesse around $\sim 2 \times 10^4$. To suppress servo bumps induced by current feedback, we amplify the cavity transmission via an

injection lock [27], whose output is further amplified by a Yb-doped fiber amplifier. The 1582 nm telecom wavelength is generated by a commercial fiber seed laser and subsequently amplified by an Er-doped fiber amplifier. Both fiber amplifiers can deliver up to 10 W of optical power.

The two amplified beams are combined in a periodically poled lithium niobate (PPLN) crystal for SFG. A portion of the generated 604 nm beam is sent to a ULE cavity to stabilize the frequency of the 1582 nm seed laser. After a power stabilization using an acousto-optic modulator (AOM), 1.5 W of 604 nm light is coupled into an SHG cavity. The SHG cavity contains a cesium lithium borate (CLBO) crystal, heated in an oven. This produces 200 mW of 302 nm UV light. We choose CLBO over beta barium borate (BBO) due to its smaller walk-off angle, which results in improved output beam quality [73]. To mitigate crystal degradation, the SHG cavity is unlocked after each experimental run and re-locked during the initial atom preparation stage.

To deliver light from the SHG cavity to the atoms with high stability, we implement several measures. A hydrogen-loaded UV fiber is used to suppress pointing fluctuations originating from the SHG cavity and upstream AOMs [74]. We also implement an intensity servo that stabilizes the UV power via an AOM that deflects excess light. Additionally, a second intensity feedback loop is applied at the final AOM using a sample-and-hold method to stabilize the pulse amplitude immediately before use.

Eight in-vacuum electrodes are used to control the electric field at the location of the tweezer array. To null the residual field, we minimize the Stark shift of the Rydberg state. Coherence between the laser and the Rydberg transition is characterized via Ramsey-type experiments (Extended Data Fig. 4b), yielding an average T_2^* coherence time of 12.8(5) μ s across the array. The observed electric field gradient is 0.62 kHz/ μ m, which is small enough to have minimal impact on gate and simulation experiments, where typical energy scales are on the order of MHz.

Extended Data Fig. 4e shows Rydberg Rabi oscillations of a single atom using this system. With loss detection, we observe 70(10) coherent Rabi oscillations before $1/e$ decay, representing the highest number of coherent spin flips observed to date in Rydberg qubits [28]. When two atoms are placed close enough for the Rydberg blockade effect, the system oscillates between $|mm\rangle$ and the entangled state $(|mr\rangle + |rm\rangle)/\sqrt{2}$. While the blockade enhances the Rabi frequency by a factor of $\sqrt{2}$, we observe loss-detected coherent cycles of 72(6) —comparable to the single-atom case— indicating that the cycle number is mainly limited by shot-to-shot intensity fluctuations [28].

For the r -qubit measurement without loss detection shown in Fig. 1, we employ auto-ionization using an inner-shell atomic transition at 369.5 nm [75]. A beam of power 1 mW is focused to a 40 μ m Gaussian waist, producing

an ionization decay time constant of 0.03 μ s, fast enough to suppress Rydberg decay prior to ionization [28].

Detection scheme of the Rydberg qubit

While in most measurements of this work, we detect the Rydberg qubits using mapping to the m -qubit and subsequently conducting the loss detectable spin measurement, some of the data in Fig. 1f relies on the direct detection of the r -qubit spin states. This was done by ionizing the Rydberg state via an auto-ionization beam [28, 75]. The ionized atoms are not trapped anymore, leave the trap and get counted as a loss while the atoms in the $|m_1\rangle$ state remain in the trap and eventually get imaged. As we show in the Extended Data Fig. 5, our ionization rate is 0.03 μ s which suppresses the Rydberg decay error during the measurement to less than 0.1%.

Rydberg state decay branching ratios

We estimate the branching ratios of the Rydberg state from various experiments shown in Extended Data Fig. 5b,c. For estimating the decay to the ground state, 1S_0 , as well as the $|m_1\rangle$ and $|m_0\rangle$ metastable state, we fitted the initial population accumulation speed with a linear fit and compared to the speed of the loss of the total Rydberg state population. To mitigate the effect of atomic loss as well as to stay in the linear part of the initial slope of the decay, we only fit the first 30 μ s of the data. The branching ratio to the $^3P_2 F = 3/2$ state is measured in a separate experiment where we compared the decayed amount to the ground state with and without the $^3P_2 F = 3/2 \rightarrow ^3S_1 F = 1/2$ repumper. Out of the ratio of those measured rates as well as the 15% decay probability to the 3P_0 state, the decay to the $^3P_2 F = 3/2$ state is identified to be 48(6)% of the decay to the 1S_0 state. Using this information we extract the final branching ratio of {42(2)%, 20(2)%, 2.7(5)%, 4(1)%} for 1S_0 , $^3P_2 F = 3/2$, $|m_1\rangle$, $|m_0\rangle$ state, remaining with an undetected population of 31(3)%. This includes the decayed portion to the other hyperfine state of $^3P_2, F = 5/2$.

Two-qubit gate calibration and error analysis

For empirical optimization of the two-qubit gate, we use one of the 20 CZ gate sequences with spin-echo pulses inserted between each pair of CZ gates as a target sequence, following Ref. [55]. We benchmark the resulting gate using echo-type global randomized benchmarking (gRB), extracting a loss-detected gate fidelity of 99.75(4)%, which is consistent with the non-echoed result presented in Fig. 3.

For the non-echoed sequence, we compensate the single-qubit phase accumulated during gate operation using an additional Z rotation. This compensation is op-

timized by maximizing the return probability of one instance of the 20-CZ non-echoed gRB sequence. For both echo and non-echo gRB, we use 40 random instances per two-qubit gate depth l .

To analyze the benchmarking data, we fit the success probability using the function $ap^l + b$, where a and p are fit parameters and l is the number of CZ gates. The asymptotic parameter b is chosen based on the detection scheme. For gRB with erasure preparation and erasure decay detection, we assume $b = 0$ since leakage from the qubit subspace dominates and results in vanishing success probability in the infinite-depth limit. For loss detection, we set $b = 1/4$, as only one of the four computational basis states $\{00, 01, 10, 11\}$ is observed per run [14, 30]. The error per gate is then extracted as $(1 - b)(1 - p)$.

To understand the sources of gate error, we perform a master equation simulation using a 16×16 density matrices with 4-levels per atom, including the states $|m_0\rangle$, $|m_1\rangle$, $|r_0\rangle$, and an auxiliary decayed state $|\text{decay}\rangle$. This state captures decay from $|r_0\rangle$ to levels outside the qubit manifold. The decay is modeled with operators $\sqrt{\Gamma_{\text{eff}}}\langle\text{decay}|r_0\rangle \otimes I$ and $I \otimes \sqrt{\Gamma_{\text{eff}}}\langle\text{decay}|r_0\rangle$ for each atom, where Γ_{eff} is derived from the branching ratio measured in Fig. 2. Decay to $|m_0\rangle$ and $|m_1\rangle$ is also included accordingly, adding up to 6 decay operators in total. This simulation scheme is also applied to the simulation of the correlated loss effect in Fig. 3.

All other imperfections are modeled as coherent errors and averaged over 1000 noise realizations. We include the following noise sources [76]:

AC intensity: Laser intensity fluctuations as time-varying Rabi frequency extracted from relative intensity noise (RIN).

DC intensity: Laser shot-to-shot intensity fluctuations as shot-to-shot Rabi frequency fluctuation sampled from gaussian noise. The standard deviation is estimated from photo-detector measurements.

Beam pointing: Laser beam pointing fluctuations are modeled as shot-to-shot Rabi frequency fluctuations sampled from Gaussian noise. The magnitude of this behavior is derived from spatial jitter observed in camera images.

Beam sampling: Atom wavepacket's finite width to the perpendicular direction of the UV laser as shot-to-shot Rabi frequency fluctuations sampled from Gaussian noise. The standard deviation is estimated from the axial temperature and tweezer width.

AC phase: Laser frequency noise. Obtained from the PDH error signal of the 604 nm laser, corrected for the ULE cavity roll-off and SHG cavity transmission characteristics, as well as by the noise scaling of the SHG.

Doppler: Error due to finite velocity of the laser direction modeled as a shot-to-shot detuning fluctuation. The standard deviation is estimated from the radial atomic temperature.

DC electric field: Constant detuning errors due to measured electric field gradient. To deduce the gate-error

result averaged over the array, detuning is sampled from a uniform distribution in the range observed in Fig. 4

To assess the expected gate fidelity, we simulate its performance on 1000 instances of m -qubit Haar-random input states. For the loss-detected case, fidelities are computed after renormalizing the state within the m -qubit manifold. The results are shown in Extended Data Fig. 6, where we find a total error of 0.35% without loss detection and 0.021% with loss detection. While we also examined the effect of tweezer position fluctuation, we find in the highly-blockaded regime, the related position error is several orders lower than the other quoted errors, therefore omitting it from the Figure.

The resulting theory values deviate by approximately 0.2% from experiment for both before and after loss detection. We hypothesize that the remaining discrepancy is likely due to imperfect convergence of the empirical optimization. In the theoretical modeling of the optimization, we numerically observe slow convergence of the gate fidelity at the 0.1% level. We leave further investigation of this effect to future work.

Population dynamics during non-Hermitian evolution

We consider the non-Hermitian state evolution in presence of Rydberg decay Γ . Initially we prepare the state $\sqrt{1 - |a|^2}|m\rangle + a|r\rangle$, which evolves to the state after non-Hermitian evolution:

$$\psi_{\text{non-H}} = \frac{\sqrt{1 - |a|^2}|m\rangle + ae^{-t\Gamma/2}|r\rangle}{\sqrt{1 - |a|^2(1 - e^{-t\Gamma})}} \quad (1)$$

Converting this equation using the initial Rydberg state population $p_0 = |a|^2$, the effective Rydberg state population in the non-Hermitian evolution is,

$$P_r(t) = \frac{p_{r0}e^{-t\Gamma}}{(1 - p_{r0}) + p_{r0}e^{-t\Gamma}} \quad (2)$$

Calibration of the anisotropic Rydberg interaction

To engineer the correct Hamiltonian in our quantum simulation experiments, precise calibration of the interaction is crucial. To perform this calibration, we directly measure the interaction between atoms using a two-photon transition to the $|rr\rangle$ state from the non-interacting $|mm\rangle$ state, with the $(|mr\rangle + |rm\rangle)/\sqrt{2}$ state as an intermediate state of the two-photon process. The detuning of such a two-photon transition resonance from the free space resonance corresponds to half of the interaction energy.

With this method, as predicted in [47], anisotropy of the Rydberg interaction is observed, depending on the inter-atomic orientation relative to the quantizing magnetic field (Extended Data Fig. 7). To achieve an effec-

tively uniform interaction, we adjust the lattice aspect ratio by 3%.

GHZ-state mapping and staggered magnetism

To map the GHZ state from the interacting r -qubit manifold to the non-interacting m -qubit manifold, we use two consecutive global π pulses on the m -qubit and on the r -qubit, as described in Fig. 2 [18]. For the second π pulse, we account for the resonance shift due to interactions between Rydberg states using a detuning of $2\pi \times 1.0$ MHz (Extended Data Fig. 9).

In Fig. 1, we use the quantity of staggered magnetism to assess the Z_2 -ordered population [29]. The staggered magnetism for the ladder geometry is defined as $M_{\text{stagger}} = \sum_{i=1,\dots,20} (-1)^i \langle \sigma_i^Z \rangle$, where the index i is defined in a circular manner around the ladder geometry and the $\sigma^Z = |0\rangle\langle 0| - |1\rangle\langle 1|$ is defined in the r -qubit. From this definition, $|M_{\text{stagger}}| = N$ only occurs when the array is showing the complete Z_2 -order, and we find a Z_2 -population summing up $M_{\text{stagger}} = \pm N$ populations.

Parity measurement of GHZ-state coherence

The GHZ fidelity of a state $\hat{\rho}$ reads

$$F = \langle \text{GHZ} | \hat{\rho} | \text{GHZ} \rangle = \frac{1}{2} (\rho_{AA} + \rho_{\bar{A}\bar{A}}) + \text{Re}(\rho_{A\bar{A}}),$$

where $|A\rangle$ and $|\bar{A}\rangle$ are the two checkerboard configurations, and $\rho_{\alpha\beta} = \langle \alpha | \hat{\rho} | \beta \rangle$. To infer the coherence term $\text{Re}(\rho_{A\bar{A}})$ following the mapping to the m -qubit manifold, we measure the parity operator $\hat{\Pi} = \prod_i \hat{\sigma}_i^Z$ after applying a global shift $\hat{U}(\phi) = \exp(-i\phi \sum_i \hat{n}_i)$ followed by a $\pi/2$ rotation $\hat{U}_x = \exp(-i\frac{\pi}{4} \sum_i \hat{\sigma}_i^X)$. As we show below, with this method, we can extract $\text{Re}(\rho_{A\bar{A}})$ from the offset of the parity oscillation rather than the amplitude. This approach differs from the standard parity-based coherence measurements requiring local control [29], and generalizes the global-control method of Ref. [77] to many-body systems.

The measured parity is given by

$$\begin{aligned} \Pi(\phi) &= \text{Tr}(\hat{U}_x \hat{U}(\phi) \hat{\rho} \hat{U}(\phi)^\dagger \hat{U}_x^\dagger \hat{\Pi}) = \\ &= \sum_n (-1)^{N_n + \frac{N}{2}} \rho_{n\bar{n}} e^{-i\phi(N_n - N_{\bar{n}})}, \end{aligned}$$

where N_n is the number of Rydberg excitations in the configuration n , and \bar{n} is the configuration where all spins in n are flipped. By taking the average over ϕ we get rid of the oscillatory terms with $N_n \neq N_{\bar{n}}$ and isolate the off-diagonal $\hat{\rho}$ components with $N_n = N_{\bar{n}}$:

$$\overline{\Pi(\phi)} = 2 \text{Re}(\rho_{A\bar{A}}) + \sum_{m \in S_A} \rho_{m\bar{m}},$$

where S_A is the set of all configurations obtained by permuting Rydberg excitations in A . From this equation,

we obtain a bound for the GHZ coherence:

$$\begin{aligned} 2 \text{Re}(\rho_{A\bar{A}}) &= \overline{\Pi(\phi)} - \sum_{m \in S_A} \text{Re}(\rho_{m\bar{m}}) \\ &\geq \overline{\Pi(\phi)} - \sum_{m \in S_A} |\rho_{m\bar{m}}| \\ &\geq \overline{\Pi(\phi)} - \sum_{m \in S_A} \sqrt{P_m P_{\bar{m}}}, \end{aligned} \quad (3)$$

where we used $|\text{Re}(x)| \leq |x|$ and the Cauchy–Schwarz inequality $|\rho_{m\bar{m}}|^2 \leq P_m P_{\bar{m}}$, with P_m the population of configuration m .

When evaluating the parity average $\overline{\Pi(\phi)}$ using a finite number of sampling points for ϕ , one must consider that $\Pi(\phi)$ contains oscillatory contributions at various frequencies. These arise from terms with configurations n and \bar{n} such that $N_n - N_{\bar{n}} = \delta N \neq 0$, leading to oscillations with period $T = 2\pi\delta N$. The corresponding amplitude is

$$A_{\delta N} = \sum_{|N_n - N_{\bar{n}}| = \Delta N} |\rho_{n\bar{n}}| \leq \sum_{|N_n - N_{\bar{n}}| = \delta N} \sqrt{P_n P_{\bar{n}}},$$

where we used the Cauchy–Schwarz inequality in the final step. From this expression, we see that oscillations with $\delta N \neq 0$ are strongly suppressed. This is because if $N_n < N/2$, then necessarily $N_{\bar{n}} > N/2$, or vice versa. As a result, at least one of the configurations n or \bar{n} must locally violate the Rydberg blockade, leading to a significantly reduced probability $P_n \ll 1$. The suppression becomes more severe with increasing δN , since larger imbalances require increasingly incompatible excitation patterns. For the GHZ state prepared using the optimal robust pulses in Extended Data Fig. 8, we estimate that the amplitude of these oscillations is small ($< 10^{-2}$) even for systems of 20 atoms.

Assuming that only the $\delta N = 2$ components contribute to the oscillations beyond the offset $\overline{\Pi(\phi)}$, any uniform sampling grid in ϕ over a 2π interval is sufficient to exactly extract the parity offset. In the experiment, we sample 11 equally-spaced values of ϕ between 0 and 2π (Extended Data Fig. 9e). The observed dependence of $\Pi(\phi)$ on ϕ in the experimental data can be attributed to two main factors: shot-to-shot geometry variations due to the fluctuations in the atomic positions that are included in our numerical simulations and discussed below, and imperfections in the overall parity measurement procedure and in the GHZ preparation that are not captured by the simulations.

In Extended Data Fig. 9g, we plot the exact GHZ coherence $2 \text{Re}(\rho_{A\bar{A}})$ for a 16-atom GHZ state, prepared using the robust pulse shown in Extended Data Fig. 8, as a function of the GHZ coherence estimated from the bound in Eq. (3). Different markers correspond to independent realizations of the fluctuating atomic positions $\mathbf{r}_i + \delta \mathbf{r}_i$, where $\delta \mathbf{r}_i$ are drawn from a gaussian distribution with zero mean and standard deviation $\delta r = 74$ nm, which is approximately 2% of the lattice spacing. In Ex-

tended Data Fig. 9h, we show the estimated GHZ coherence as a function of δr , for δr up to 111 nm. For each disordered instance, the lower bound in Eq. (3) is nearly saturated, indicating that the parity offset serves as a reliable estimator of GHZ coherence. However, positional disorder—though partially mitigated by the robust pulses—still induces significant shot-to-shot fluctuations in the exact GHZ coherence, accounting for the large experimental error bars.

Optimal control for GHZ-state preparation

The GHZ-state preparation pulse is optimized using the Gradient Ascent Pulse Engineering (GRAPE) algorithm [78]. The control parameter $\Delta(t)$ is discretized on a time grid of $N = 150$ points $t_j = (j + \frac{1}{2})dt$, $j = 0, 1, \dots, N - 1$, with $dt = T/N$, and T the total evolution time, such that $\Delta_j = \Delta(t_j)$ are the variational parameters of the optimization. The Rabi frequency $\Omega(t)$ is fixed to a cosine-tapered window function (cf. Fig. 4c). The cost function is defined as the preparation infidelity averaged over N_s realizations of the fluctuating geometry:

$$C = 1 - \frac{1}{N_s} \sum_{k=1}^{N_s} \left| \langle \text{GHZ} | \prod_{j=0}^{N-1} e^{-idt\hat{H}^{(k)}(\Delta_j)} | mm \dots m \rangle \right|^2, \quad (4)$$

where $\hat{H}^{(k)}(\Delta_j)$ is the many-body Rydberg Hamiltonian with atoms at positions $\mathbf{r}_i + \delta\mathbf{r}_i^{(k)}$, with \mathbf{r}_i are the ladder coordinates. To ensure the smoothness of the optimal control function $\Delta(t)$, we add a penalty term to the cost function: $C \rightarrow C + \eta \int_0^1 ds (d\Delta/ds)^2$, where $s = t/T$ and $\eta = 10^{-3}$. In the numerical optimization, $N_s = 30$ and $\delta\mathbf{r}_i^{(k)}$ are drawn from a gaussian distribution with zero mean and standard deviation $\delta r = 60$ nm. We verified that the resulting optimal pulses are independent of the number of samples and on δr . The optimization is performed using a gradient-based algorithm, where the gradient can be efficiently computed from the approximation $\partial\hat{U}_j/\partial\Delta_j \simeq -idt\partial\hat{H}(\Delta_j)/\partial\Delta_j\hat{U}_j$. The optimization process begins with a short total evolution time T and a linear profile for $\Delta(t)$ as the initial guess. Upon convergence, T is incrementally increased as $T \rightarrow T + dT$, and the optimized profile at total time T is used as the initial guess for the optimization at total time $T + dT$.

Effect of the Rydberg decay detection

Our decay-detection capabilities enable us to infer an effective Rydberg lifetime of 1.2(2) ms. However, it is not a priori guaranteed that the post-selected dynamics (conditioned on no detected decay events) is equivalent to the dynamics of a system with such an extended lifetime. To clarify this, we compare the ideal unitary (no-

decay) evolution with the post-selected (no-jump) dynamics, which is governed by the effective non-hermitian Hamiltonian $H = H_0 - \frac{i}{2} \sum_j n_j$, where the state is normalized after each time step. As shown in Extended Data Fig. 10, the resulting no-jump dynamics reproduces the ideal unitary evolution with high accuracy even for decay rates up to an order of magnitude larger than the experimental condition, confirming that the observed dynamics faithfully represents coherent GHZ-state preparation. In the same figure, we also explore the quench dynamics under a time-independent Hamiltonian at zero Rydberg detuning, showing larger but still limited deviations between the no-jump and ideal unitary dynamics under the present experimental conditions.

We note, however, at much larger decay rates the no-jump dynamics deviates significantly from the purely unitary case. In this regime, experiment reflecting the feature of non-Hermitian quantum dynamics can be realized, such as enhanced evolution of the correlation, provided that decay rates can be artificially engineered and sufficient post-selection statistics are maintained [66, 67].

Error bars and fitting

Error bars on populations and parity measurements are 68% Clopper-Pearson confidence intervals. Fits of the experimental data are done using weighted least squares and error bars on fitted parameters represent one standard deviation fit errors.

Acknowledgements

We acknowledge discussions with A. Cao, G. Liu, M. Peper, and J. D. Thompson; technical input from W. Eckner, C. Gross, P. Osterholz, F. Rönchen F. Vietmeyer, A. Wilson; and, comments on the manuscript from N. Darkwah-Oppong, J. Thompson, D. Young and Y. Zhan.

A.B. is supported by the Swiss National Science Foundation under grant 222216. G. G. acknowledges support from the European Union's Horizon Europe program under the Marie Skłodowska Curie Action TOPORYD (Grant No. 101106005). These results are based upon work supported by the Office of Naval Research (N00014-23-1-2533), Air Force Office of Scientific Research (FA9550-23-1-0097), Army Research Office / LPS (W911NF24S0004), U.S. Department of Energy, Office of Science, National Quantum Information Science Research Centers, Quantum Systems Accelerator, NSF Convergence Accelerator, the NSF QLCI Award OMA - 2016244, Physics Frontier Center PHY-2317149, the National Institute of Standards and Technology, the ERC Starting grant QARA (Grant No. 101041435), the Horizon Europe programme HORIZON-CL4-2022-QUANTUM02-SGA via the project 101113690 (PASQuanS2.1) and by the Austrian Science Fund (FWF) (Grant No. DOI 10.55776/COE1).

Note: While completing this work, we became aware of complementary work on erasure enhanced quantum error correction utilizing ^{171}Yb metastable qubit [79].

Author Contributions

A.S., A.B., J.W.L., G.M.V., and A.M.K. contributed to the experimental setup, performed the measurements, and analyzed the data. Z.Z., G.G., and H.P. theoretically developed the disorder-robust pulses and the GHZ-state coherence measurement method with global control. A.M.K. and H.P. supervised the work. All authors contributed to the manuscript.

Competing Interests

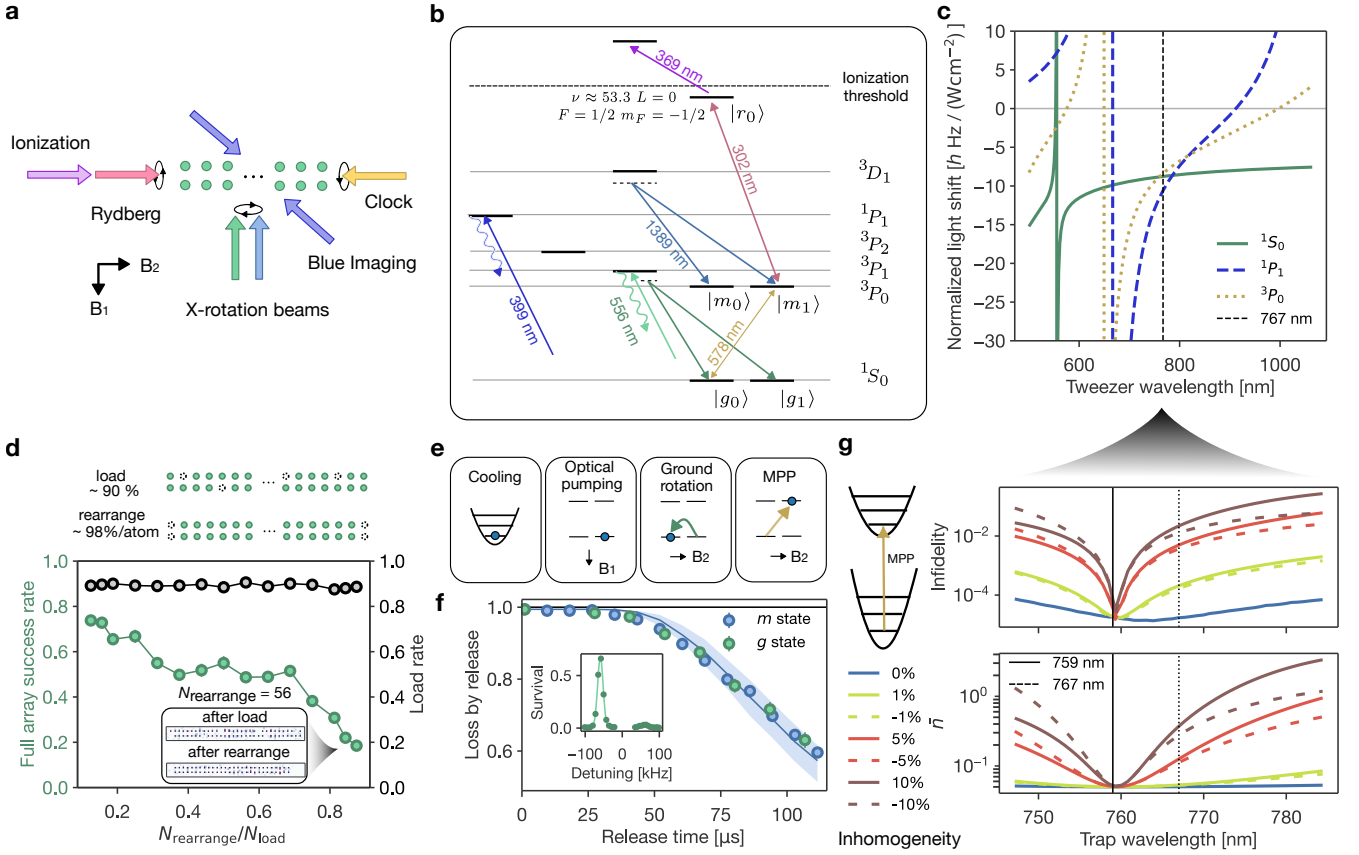
The authors declare no competing interests.

Materials and Correspondence

Correspondence and requests for materials should be addressed to A.M.K.

Data Availability

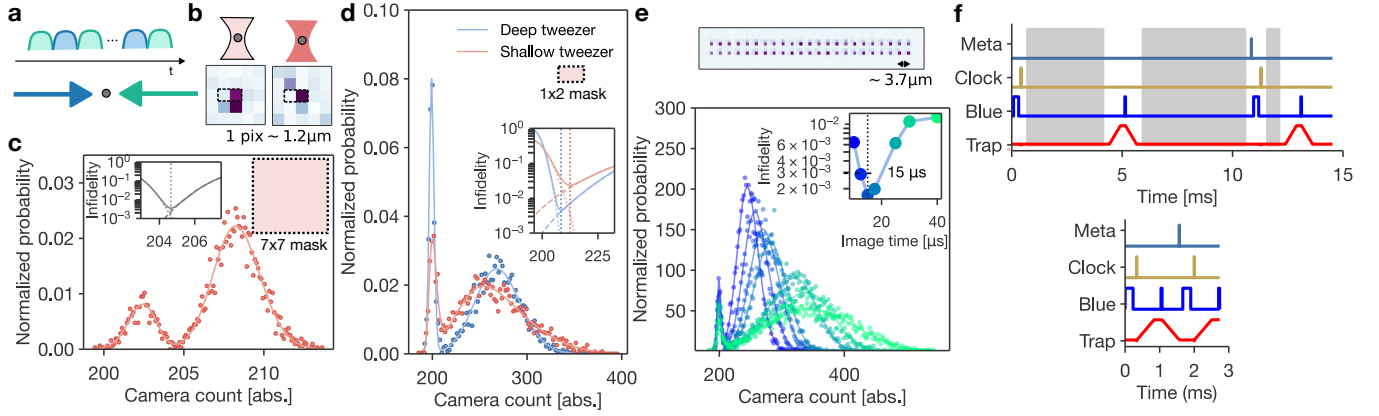
The data that support the findings of this study are available from the corresponding author upon reasonable request. Source data for figures 1–4 are provided with the paper.



Extended Data Fig. 1. **Beam geometry, atomic structure, tweezer polarizability, resource-efficient rearrangement, and state preparation.** **a**, Beam and magnetic field geometry relative to the atom array. B_1 is used during initial optical pumping and Raman cooling, followed by B_2 for the qubit manipulations. The X-rotation beams for both the ground and metastable states propagate perpendicular to B_2 . The Rydberg and clock beams are aligned parallel to the magnetic field and use circular polarization to drive the σ^+ transition. The ionization beam is co-aligned with the UV beam. **b**, Atomic structure of ^{171}Yb showing the transitions relevant to the experiment. The 1P_1 transition is used for fast destructive imaging, while 3P_1 serves as both the non-destructive imaging transition and the intermediate state for Raman transitions. The metastable state is coupled to the Rydberg state via a single-photon transition. The ionization beam is resonant with an inner-shell transition. **c**, Polarizability of excited states compared to the ground state 1S_0 . At the operational tweezer wavelength 767 nm, the 3P_0 state is nearly magic, and the 1P_1 state used for destructive imaging remains trapped. For 1P_1 , only the scalar polarizability is considered due to scattering from both magnetic sublevels. **d**, Enhanced loading and rearrangement. We use single-atom loading at an efficiency of $\sim 90\%$ followed by rearrangement to prepare defect-free arrays, as illustrated in the top graphic. The data show the full-array success rate as a function of target array size. **e**, State preparation sequence to the metastable state. After preparing the radial motional ground state via Raman sideband cooling, we flip the spin in the ground-state manifold using a π -pulse. Motional-state-preserving pulses (MPPs) are used to coherently excite the atoms to the 3P_0 state without adding motional excitation[13]. **f**, Measurement of atomic temperature. The inset: sideband spectroscopy indicating $\bar{n} = 0.05$. Main panel: release-and-recapture comparison between ground and metastable states. The agreement shows that the clock excitation does not introduce additional motional heating. The solid line shows the Monte-Carlo simulation best agrees with the experiment. We extract the atomic temperature of $0.28(4) \mu\text{K}$. **g**, Simulation results for motional-state-preserving pulses at varying wavelengths. The upper panel shows the population transfer infidelity; the lower panel shows the motional excitation added by the pulse, indicating heating.

Extended Data Table. I. **Detection probability of the three outcome measurement.** This table provides the numerical values corresponding to the data shown in Fig. 2b. While preparation erasure detection is applied, we do not correct for spin preparation errors arising from the π -pulse in the metastable state manifold used to prepare $|m_0\rangle$.

Prepared	$ m_1\rangle$ observed	$ m_0\rangle$ observed	Loss observed
$ m_1\rangle$	96.9(2) %	0.18(6) %	2.8(2) %
$ m_0\rangle$	0.70(10)%	94.9(2) %	4.3(2) %
Non	0.02(3)%	0.02(3)%	99.97(3)%



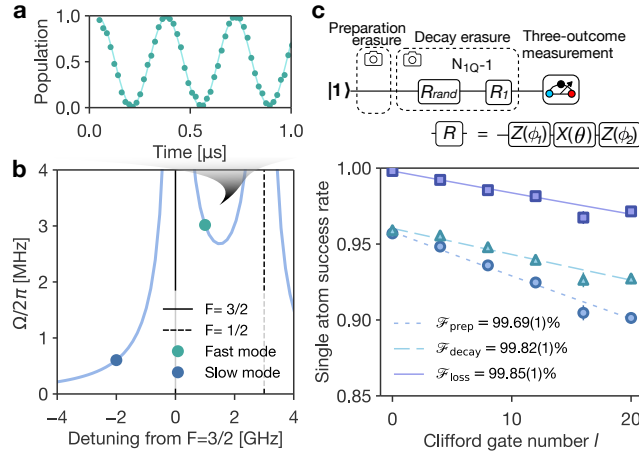
Extended Data Fig. 2. **Blue imaging and experimental sequence for the three-outcome measurement.** **a**, Beam geometry and sequence of the destructive imaging. Counter-propagating beams resonant with the 1S_0 to 1P_1 transition are alternately applied on the atoms at a frequency of 3 MHz. **b**, Two methods of fast imaging. We use either 250 kHz-deep tweezers (“shallow”) or 9.6 MHz-deep tweezers (“deep”) in the experiment. The shallow tweezers are used for erasure detection, while the deep tweezers are used for spin detection. Bottom: typical single-shot images from both methods. The deep tweezers confine the atom position more tightly. **c**, Photon count histogram from shallow-tweezer imaging using a 7×7 pixel region of interest (ROI). A two-Gaussian fit infers a spin-readout infidelity below $< 0.5\%$. **d**, Comparison of photon count histograms from deep and shallow tweezers using a small ROI. The deep tweezers result in reduced overlap due to better confinement. **e**, Optimization of imaging time in a tightly spaced array matching the GHZ experiment geometry (Top). As imaging time increases, infidelity initially decreases due to improved fluorescence collection, then increases beyond $15 \mu\text{s}$ due to cross-talk from neighboring atoms. A similar trend is observed in the geometry for the gate experiment, which uses even smaller atom spacing ($2.4 \mu\text{m}$). **f**, Three-outcome imaging sequence. “Meta” represents the π -pulse on the m -qubit subspace. The π -pulse on the o -qubit is indicated as “Clock”. “Blue” indicates application of the resonant beam to the $^1S_0 \leftrightarrow ^1P_1$ transition, used for both, imaging and blow-away of ground-state atoms. (Top) Actual experimental sequence, with wait times inserted for camera readout. (Bottom) Projected sequence duration, totaling less than 3 ms.

Extended Data Table. II. **Preparation error summary.** Errors from individual preparation steps, extracted from experimental measurements and/or calculations. Experimentally characterized (calculated) errors are indicated by [e] ([c]). The listed errors can largely be separated into those that are detectable via erasure and those that are not. The third column indicates spin-flip errors that occur during a state preparation step. The last two rows show the additional preparation error that occurs if one prepares $|m_0\rangle$.

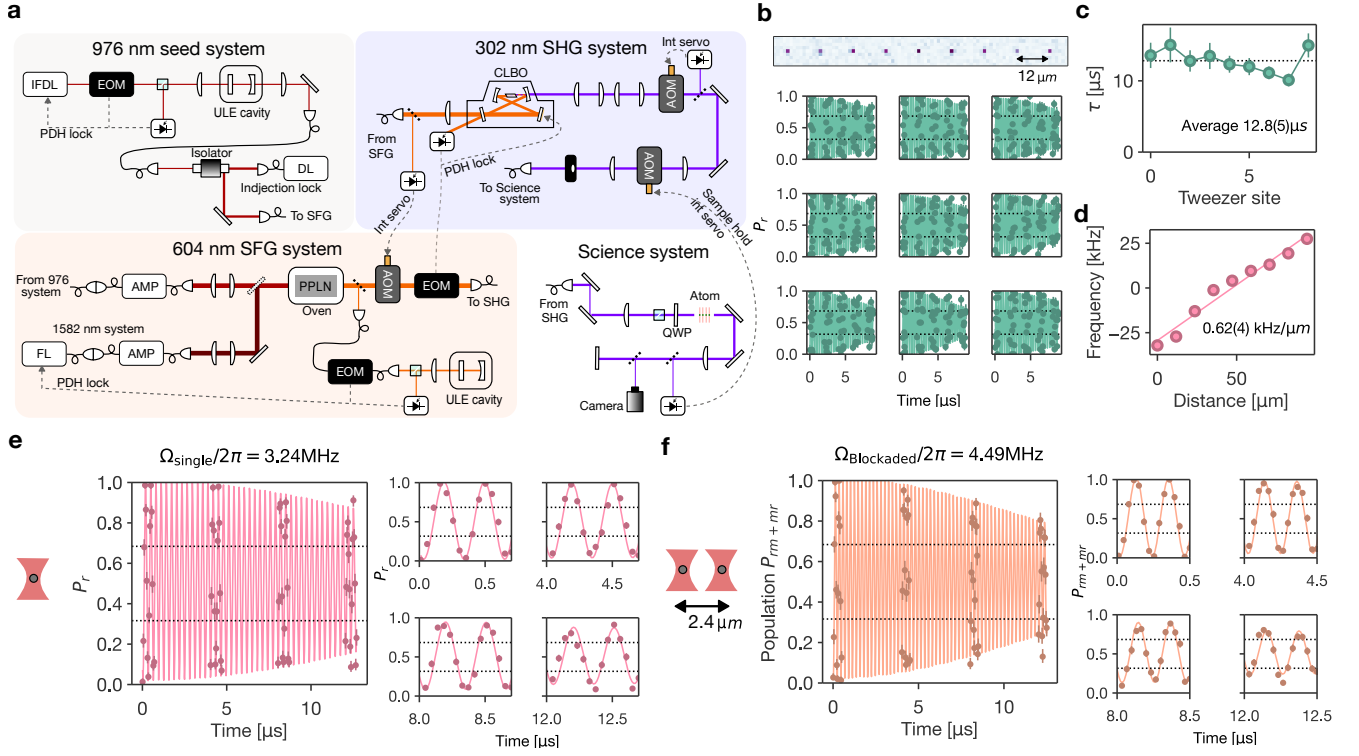
Preparation step	Loss Error	Erasure corrected	Spin flip error
Imaging loss [e]	0.4(1) %	0.4(1) %	-
g -qubit π -pulse [e]	0.9(1)%	$< 0.02\%$	-
Tweezer ramp down [e]	0.4(1)%	0.4(1)%	-
o -qubit MPP (σ^+ -pol) [e]	0.4(1)%	$< 0.01\%$	-
o -qubit MPP (π -pol.) [e]	-	-	0.19(6)%
Total $m_1\rangle$	2.1(2)%	0.8(1)%	0.19(6)%
m -qubit π -pulse [e+c]	0.56(1)%	0.38(1)%	0.38(1)%
Total $m_0\rangle$	2.7(2)%	1.2(1)%	0.57(6)%

Extended Data Table. III. **Readout error summary.** Errors from individual readout steps, extracted from separate measurements. Experimentally characterized (calculated) errors are indicated by [e] ([c]). Each error contributes either to atom loss (“Loss error”) or to spin mislabeling (“Spin misl. error”), where spin mislabeling refers to the incorrect assignment of a spin state. The final two columns indicate how each error source affects the first and second spin readouts, respectively.

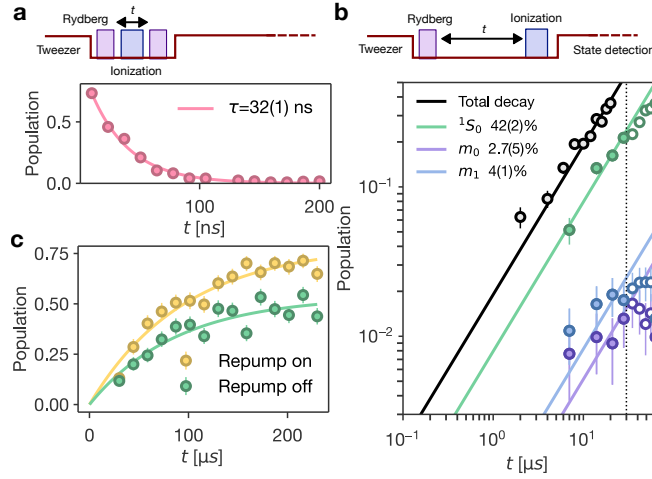
Readout step	Loss Error	Spin misl. Error	Readout $ m_1\rangle$	Readout $ m_0\rangle$
Release and Recapture [e]	0.3(1) %	-	1x	2x
o -qubit π -pulse (π -pol) [e/c]	x	0.10(3) %	0x	1x
o -qubit π -pulse (σ^+ -pol) [c]	0.4(1)%	-	1x	1x
m -qubit π -pulse [e]	0.56(1)%	-	0x	1x
Destructive image infidelity [e]	0.2(1)%	-	1x	1x
Raman scattering deep tweezer [c] ($^1S_0 + ^3P_0$)	0.13(1)%	-	0x	1x
Raman scattering hold (per ms) [c] ($^1S_0 + ^3P_0$)	0.005(1)%	-	5x	13x
Vacuum loss (per ms)[c]	0.00026(1)	-	5x	13x
Total readout loss/ Spin misl. [%]			0.9(2)/0.0	1.9(2)/0.10(3)
Preparation Error [%]			0.8(1)/0.19(6)	1.2(1)/0.57(6)
Total loss/ Spin misl. [%]			1.7(2)/0.19(6)	3.1(2)/0.7(1)



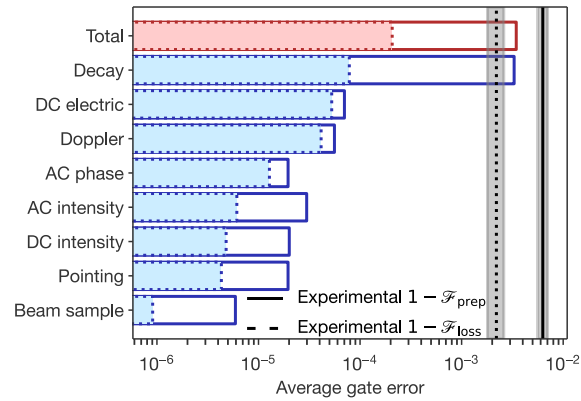
Extended Data Fig. 3. **Single-qubit control.** **a**, Fast Rabi oscillations on the metastable-state qubit, as used for mapping from the Rydberg state. The fit yields a Rabi frequency of $2\pi \times 2.9$ MHz. **b**, Calculated dependence of the Rabi frequency on detuning, at constant laser power. When high speed is not required—such as in global randomized benchmarking (gRB) of the two-qubit gate—we use a slower Rabi frequency by increasing the detuning, in order to reduce intermediate-state scattering and mitigate the finite AOM turn-on time. **c**, Single-qubit Clifford randomized benchmarking comparing erasure and three-outcome measurement schemes. To reduce scattering errors, Z -rotations are implemented via phase tracking.



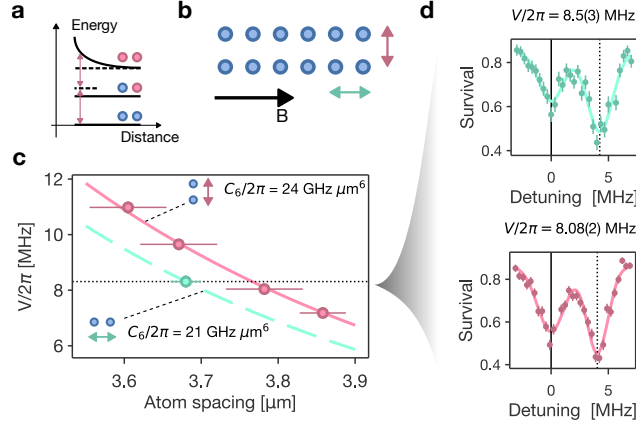
Extended Data Fig. 4. **Rydberg laser system and coherent manipulation of the Rydberg state.** **a**, UV laser system. We use fiber lasers (FL) and diode lasers (DL) as seed sources, which are amplified using fiber amplifiers (AMP). High-power beams are then combined via sum frequency generation (SFG) and frequency-doubled using second harmonic generation (SHG) to produce several hundred milliwatts of UV light. To suppress frequency noise, the cavity transmission of a high-finesse ($\mathcal{F} \approx 2 \times 10^4$) ultra-low-expansion (ULE) cavity is used to seed the 977 nm system [27]. A PPLN crystal is used for SFG of the 977 nm and 1582 nm beams, generating 604 nm light, which is then frequency-doubled in an SHG cavity containing a CLBO crystal. To extend the crystal lifetime, the SHG cavity is unlocked between experiments, stopping UV generation. Electro-optic modulators (EOMs) are used for all laser frequency locks. UV intensity stabilization is achieved via servo control of both the 604 nm and final 302 nm beams. A sample-and-hold feedback scheme is used to suppress shot-to-shot pulse fluctuations. **b**, T_2^* coherence assessment of the Rydberg transition. Atoms are spaced for about $12 \mu\text{m}$, and a Ramsey sequence is performed with a detuning offset of 3 MHz applied during the dark time. **c**, Observed coherence time across the tweezer array, with an average of $12.8(5) \mu\text{s}$. **d**, Variation of the oscillation frequency across the array reveals an energy gradient of $0.62 \text{ kHz}/\mu\text{m}$. **e**, Single-atom Rydberg Rabi oscillations on the r -qubit under loss detection. We observe $70(10)$ coherent oscillations before $1/e$ decay. **f**, Rydberg Rabi oscillations under blockade. Due to interaction, the Rabi frequency is enhanced by a factor of $\sqrt{2}$ compared to the non-interacting case. We observe $72(6)$ coherent oscillations before $1/e$ decay.



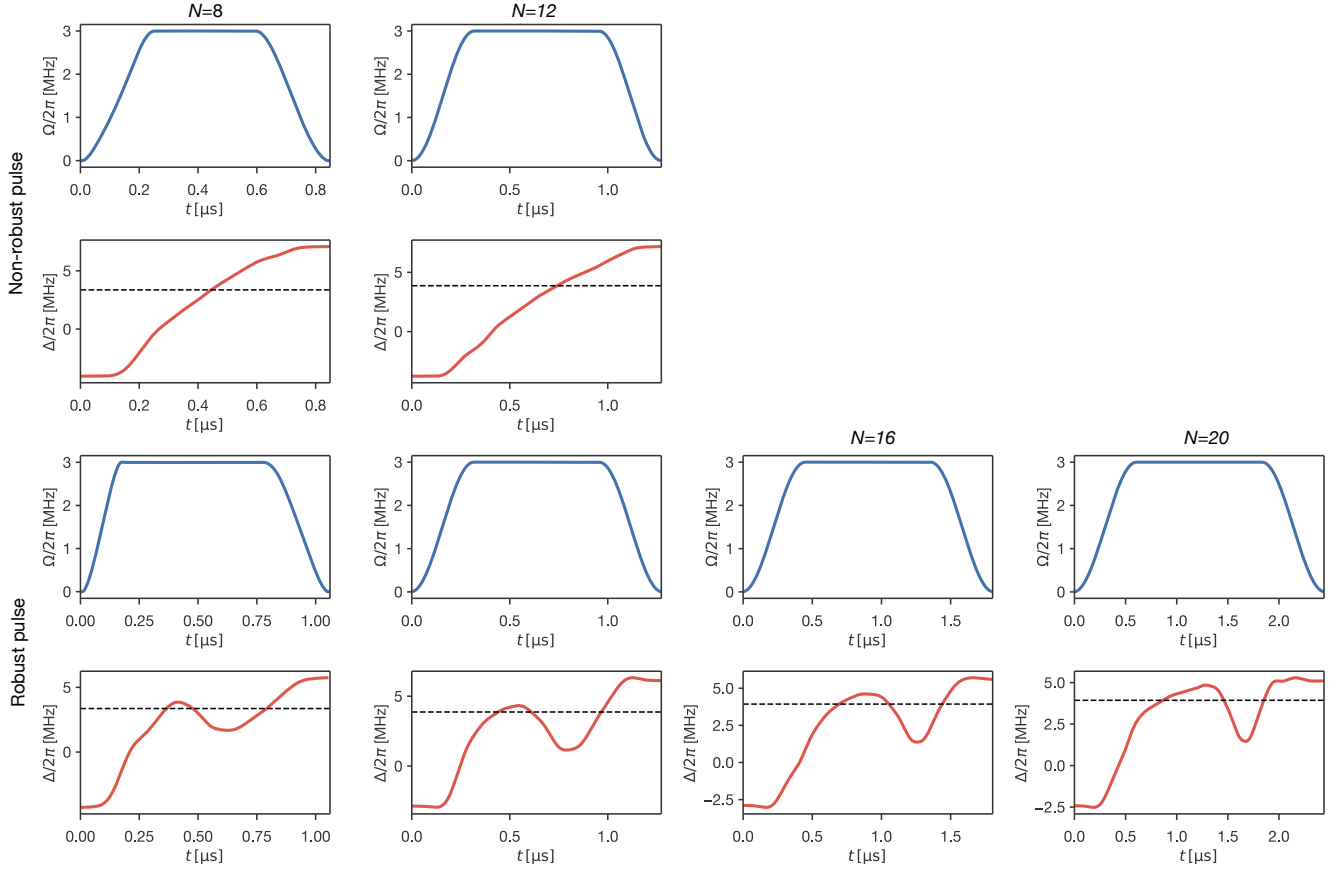
Extended Data Fig. 5. **Auto-ionization and Rydberg state decay branching.** **a**, Characterization of the population decay, varying the ionization pulse duration in between the π -pulses for the Rydberg transition. The solid line is an exponential fit. **b**, Characterization of the branching of the decayed Rydberg state to ground state and metastable state. Black lines are total amount of decay measured by two consecutive Rydberg π -pulses. Remaining branching is measured by the sequence shown on top of the graphic, where we changed the timing of the ionization of the Rydberg state and measured the amount of the remaining population. **c**, Assessment of the branching to the $^3P_2 F = 3/2$ state. Decay experiments by monitoring the ground state. In one case we apply a 770 nm repump laser resonant with the $^3P_2 F = 3/2 \rightarrow ^3S_1$ transition, and in another case we do not apply the repumper. The ratio of the two experiments allow us to estimate the decay population to $^3P_2 F = 3/2$.



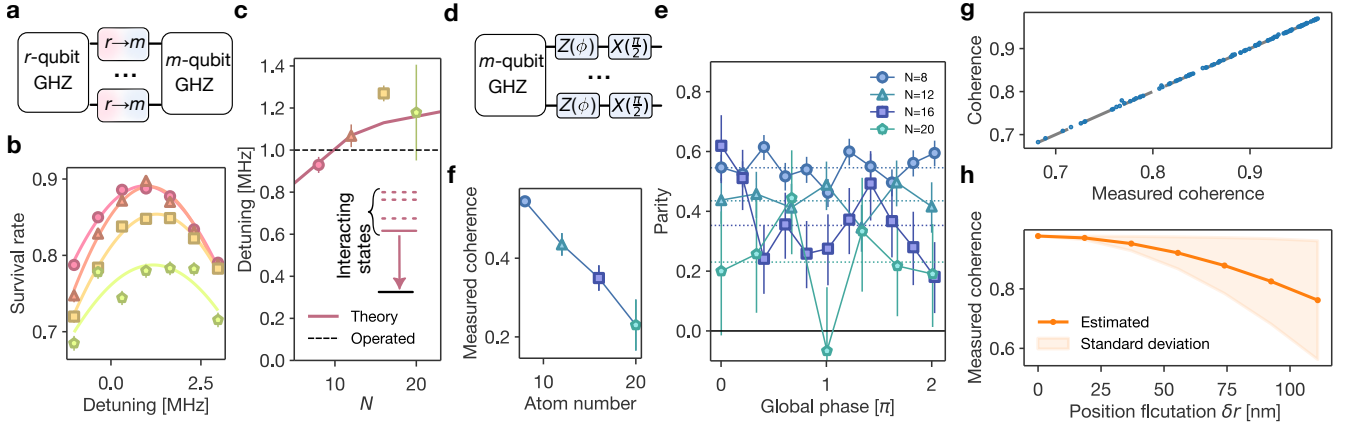
Extended Data Fig. 6. **Two-qubit gate error assessment.** Theoretical assessment of known error contributions. Simulated gate infidelities are shown both without loss detection (solid bars) and with loss detection (dotted bars). The top row presents the average gate fidelity from full error-model simulations. Individual error sources are ordered by their contribution to the loss-detected error. We also show the experimental result from Fig. 3 with vertical lines.



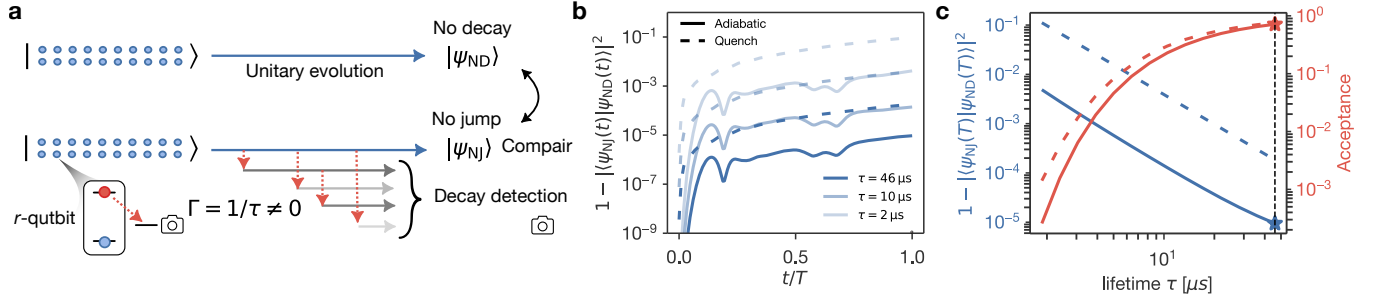
Extended Data Fig. 7. **Rydberg interaction calibration.** **a**, For the interaction calibration, we use a two-photon transition to the doubly excited state. **b**, As reported on [47], we observe an anisotropy of the interaction depending on the orientation of the interaction axis relative to the magnetic field. Adjusting the atom distances effectively generates the square lattice interaction. **c**, Result of the anisotropy calibration. Showing higher interaction strength for the direction perpendicular to the magnetic field. **d**, The interaction spectroscopy result after calibrating the lattice geometry. Residual imbalance is caused by the limited SLM discretization, which can be solved by using more computational resources.



Extended Data Fig. 8. **Implemented optimal control pulse.** Rabi frequency (top) and detuning (bottom) sweep profiles are shown for both robust and non-robust pulses implemented in Fig. 4. The dotted line is a theoretically estimated phase transition point.



Extended Data Fig. 9. **Qubit mapping of the Z_2 -GHZ state and assessment of the coherence.** **a**, Schematic of the qubit mapping of the Z_2 -GHZ state. **b**, To achieve maximum mapping efficiency a detuned π -pulse is used for the mapping. **c**, Summary of the relation between atom number and optimal detuning. We choose $2\pi \times 1.0$ MHz for all of the experiments. The inset shows the schematic of the qubit mapping. **d**, Schematic of the sequence for the assessment of the GHZ coherence. After mapping to the non-interacting metastable state qubit, we apply a global $\pi/2$ -pulse with various phases. **e**, Result of the parity measurements for the GHZ coherence assessment. We estimate the coherence of the GHZ state by averaging the observed parity expectation values after a global phase shift, over the interval 0 to 2π . **g**, Theoretical comparison of actual coherence and estimated coherence by the presented method. **h**, GHZ coherence for various distance fluctuations. δr is the standard deviation of the Gaussian distribution of the shot-to-shot position fluctuations.



Extended Data Fig. 10. **Analysis of the effect of decay detection on the many-body preparation dynamics.** **a**, Concept of the simulation. We theoretically compare the many-body evolution in the case of no Rydberg decay (ND) and the case of finite Rydberg decay and perfect decay detection. The latter dynamics is equivalent to the evolution generated by an effective non-Hermitian Hamiltonian describing the no-jump (NJ) component of the dissipative process. We vary the magnitude of the decay rate and examine how the prepared states deviate from the no-decay case by computing the infidelity $1 - |\langle \psi_{\text{NJ}} | \psi_{\text{ND}} \rangle|^2$. **b**, Infidelity during the evolution for various decay rates. For the adiabatic evolution (solid lines), we analyze the many-body evolution generating a 20-atom GHZ state with the robust preparation protocol for $\Omega T = 46$. This is what is used for the $N = 20$ GHZ state in Fig. 4. For the quench evolution (dashed lines), we set zero Rydberg detuning and constant Rabi frequency at $2\pi \times 3$ MHz. **c**, Infidelity at the end of the preparation. The vertical dashed line ($\tau = 46 \mu\text{s}$) denotes the Rydberg state lifetime in the present experiment. Stars indicate the condition implemented in the GHZ generation experiment.